Naval Research Laboratory

Washington, DC 20375-5320

NRL/MR/6394--16-9690

Validation of Temperature Histories for Structural Steel Welds Using Estimated Heat-Affected-Zone Edges

S.G. LAMBRAKOS

Center for Computational Materials Science
Materials Science and Technology Division

October 12, 2016

REPORT DOCUMENTATION PAGE

Form Approved
OMB No. 0704-0188

1. REPORT DATE *(DD-MM-YYYY)*	**2. REPORT TYPE**	**3. DATES COVERED** *(From - To)*
12-10-2016	NRL Memorandum Report	

4. TITLE AND SUBTITLE

Validation of Temperature Histories for Structural Steel Welds Using Estimated Heat-Affected-Zone Edges

5a. CONTRACT NUMBER

5b. GRANT NUMBER

5c. PROGRAM ELEMENT NUMBER

6. AUTHOR(S)

S.G. Lambrakos

5d. PROJECT NUMBER

5e. TASK NUMBER

5f. WORK UNIT NUMBER
63-0000-00

7. PERFORMING ORGANIZATION NAME(S) AND ADDRESS(ES)

Naval Research Laboratory, Code 6394
4555 Overlook Avenue, SW
Washington, DC 20375-5320

8. PERFORMING ORGANIZATION REPORT NUMBER

NRL/MR/6394--16-9690

9. SPONSORING / MONITORING AGENCY NAME(S) AND ADDRESS(ES)

Office of Naval Research
One Liberty Center
875 North Randolph Street, Suite 1425
Arlington, VA 22203-1995

10. SPONSOR / MONITOR'S ACRONYM(S)

ONR

11. SPONSOR / MONITOR'S REPORT NUMBER(S)

12. DISTRIBUTION / AVAILABILITY STATEMENT

Approved for public release; distribution is unlimited.

13. SUPPLEMENTARY NOTES

14. ABSTRACT

Temperature histories of structural steel deep-penetration welds are presented, which are calculated using numerical-analytical basis functions and solidification-boundary constraints. These weld temperature histories can be adopted as input data to various types of computational procedures, which include numerical models for prediction of solid-state phase transformations and mechanical response. In addition, these temperature histories can be used parametrically for inverse thermal analysis of welds corresponding to other welding processes whose process conditions are within similar regimes. The present study applies an inverse thermal analysis procedure that uses three-dimensional constraint conditions whose two-dimensional projections are mapped within transverse cross sections of experimentally measured solidification boundaries. In addition, the present study uses experimentally measured estimates of the heat-affected-zone edge to examine the consistency of calculated temperature histories for steel welds.

15. SUBJECT TERMS

Inverse thermal analysis Welding
Stainless steel

16. SECURITY CLASSIFICATION OF:			**17. LIMITATION OF ABSTRACT**	**18. NUMBER OF PAGES**	**19a. NAME OF RESPONSIBLE PERSON**
					Samuel G. Lambrakos
a. REPORT	**b. ABSTRACT**	**c. THIS PAGE**	Unclassified Unlimited	58	**19b. TELEPHONE NUMBER** *(include area code)*
Unclassified Unlimited	Unclassified Unlimited	Unclassified Unlimited			(202) 767-2601

Standard Form 298 (Rev. 8-98)
Prescribed by ANSI Std. Z39.18

Contents

Introduction

Thermal analysis of welds seeks to determine the temperature history, i.e., change in temperature with time, at positions on weld cross sections [1,2]. Given temperature histories as a function of cross section position, observed weld microstructure and weld performance can be correlated with rates of temperature change during welding, and residual strains within welds can be predicted using models for which temperature histories are input quantities. The direct-problem or first-principles approach for estimation of tempeature histories entails solving the coupled transport equations using numerical methods based either on finite differences or finite volumes [3,4]. This approach has the advantage of providing insight concerning the relationship between weld characteristics and underlying physical processes, i.e., the nature of workpiece and energy source coupling. For controlled welding experiments, where weld meltpool morphology is simple and thermocouple measurements are available, the direct problem approach can be used for determination of material properties. This would entail adjustment of model parameters to achieve agreement between predicted and measured temperature histories at thermocouple locations. The direct problem approach, however, has many disadvantages for practical weld thermal analysis, which are as follows.

Direct-problem based models, which are formulated in terms of basic theory, are difficult to apply for quantitative weld analysis in that most material properties needed for this type of modeling are not available. Weld meltpool morphologies can in general be extremely complex due to the wide variety and complexity of welding processes, e.g., hybrid welding processes. Direct-problem based models are not structured to adopt as input detailed information concerning complex shapes of weld meltpools. That is to say, the detailed modeling of underlying physical processes resulting in complex meltpool morphologies is in practice not feasible. Direct-problem based models are not structured to adopt thermocouple measurements as input, but rather only as verification of model output. Finally, direct-problem based models, by their nature, are in general not structured for modeling “overdetermined-systems” [4], i.e., weld thermal analysis where relatively many experimental measurements are available, e.g., shape features of solidification boundaries and thermocouple measurements. Accordingly, with respect to direct-problem based modeling, experimental measurements may not be adaptable as model-input information or be useful only for model verification.

In contrast to the direct-problem approach, the inverse-problem approach [5-7] for weld thermal analysis, using parametric functions of minimal complexity, has many advantages for quantitative estimation of weld temperature histories [8-19]. This approach entails calculation of temperature fields within the volume of the workpiece using parametric functions that are structured for convenient parameter adjustment with respect to detailed information obtained from measurements, such as solidification boundaries and thermocouple measurements. The concept of system representation using “minimally complex” parametric functions is related to that of system representation using linear combination of basis functions [4], which follows the analysis approach of signal processing, where analysis is in terms of the superposition of fundamental modes of system response [20]. Following this approach, a system’s response, no matter how complex, is decomposed into a linear combination of component contributions whose formal structure are characteristic modes of that system. For example, in the case of signal processing of transmitted waves, e.g., electromagnetic or acoustic, the characteristic modes are sine and cosine functions, which represent in principle the simplest parameterization in terms of basis functions for inverse analysis. Similarly, in the case of inverse thermal analysis, the characteristic modes are the kernel and fourier series

Manuscript approved August 15, 2016.

solutions to the heat condunction equation, representing the simplest parametrization in terms of basis functions [21]. It follows that the inherent complexity of any numerical procedure for inverse models formulated in terms of linear combinations of basis functions should be significantly less than those for applying models based on first principles, i.e., transport equations, such as finite-element and finite volume procedures [3,4]. In addition to being physically consistent basis functions for parametric representaion of weld temperature fields, the kernel and fourier series solutions to the heat condunction equation have general functional forms that are sufficiently flexible so as not to impose any form of model bias on calculated temperature histories. The mathematical foundation of inverse thermal analysis using linear combinations of basis functions is that of least-squares parameter optimization [4,22,23].

Inverse analysis compensates for lack of information concerning material properties and complex physical processes associated with energy source and workpiece coupling [24-27]. The goal of welding models formulated in terms of basic theory, inclusing those of deep-penetration welding, is simulation of the coupling of the heat source, which involves melting, fluid flow in the weld meltpool and heat transfer from the solidification boundary into the heat affect zone (HAZ). With respect to practical analysis, the purpose of modeling these influences, in particular, would be generation of the solidification boundary, the surface from which heat is transferred into the HAZ, which is the region of most probable weld failure, and difficult for inspected. Therefore, inverse models that adopt weld cross sections of solidification boundaries as "model input" should tend to compensate for lack of information concerning physical processes occuring within the melt pool. This reasoning also applies to physical processes occuring within the mushy zone. With respect to inverse analysis, measured solidification boundaries represent estimates of mushy-zone edges, which are at the solidus temperature.

Presented here is a case study inverse thermal analysis of structural steel deep-penetration welds. This analysis provides a parameterization of temperature histories for prediction of properties within the HAZ of welds for the regime considered. The present study applies an inverse thermal analysis procedure that uses volumetric constraints on calculated three-dimensional solidification boundaries. These constraints are such that two-dimensional projections of calculated solidification boundaries are constrained to fall within measured solidification cross-section boundaries. For the present study, which considers deep-penetration welds of structural steel, inverse thermal analysis includes prediction of temperature histories at experimentally estimated HAZ-edges. The parametric temperature histories presented in this study can be adopted for inverse thermal analysis of welds corresponding to other process parameters or welding processes whose process conditions are within similar regimes. Further, this study can contribute to a parameter space for inverse themal analysis, which contains a wide range of parameters corresponding to different welding processes, process conditions and different types of metals and their alloys.

The inverse analysis procedure applied here entails parametric representation of the temperature field in terms of numerical-analytical basis functions [24-27], which consist of numerical integrals of analytic functions over time. The conceptual foundation of this procedure was introduced in reference [28]. The parametric representation provides a general reduction of model complexity for purposes of weld thermal analysis. Reduction of model complexity is achieved by adopting numerical-analytical models for either the heat source or temperature field (or both) in combination with numerical methods. Among studies applying this approach are [2, 29-35].

The present study contributes to a parameter space relating shapes of weld solidification boundaries, or shapes of any specified boundaries within the weld, to weld temperature histories, as well as to weld process parameters. The inverse analysis methodology applied here, which permits

convenient adjustment of parameters, uses discrete source distributions. These source distributions, consisting of a finite number of point sources distributed in three-dimensions, are conveniently adjustable with respect to location and source strength for calculation of temperature fields on and exterior to specified isothermal boundaries, e.g., solidification boundaries (see reference [24-27]). The use of discrete source distrubutions in this study, which are within three dimensions (i.e., volumetric), is formally equivalent to the Myhr-Grong method [30], which typically employs discrete source distributions within two-dimensional planes transverse to the relative motion of heat source and workpiece. References [34,35], and reference therein, demonstrate the use of discrete source distributions for numerical modeling of transport phenomena associated with welding processes.

An important part of the present study, which extends the methodology for inverse thermal analysis, is examination of a procedure accessing the consistency of calculated temperature histories for steel welds, which uses experimentally measured estimates of the HAZ edge. In order to demonstrate practical application of this procedure, as well as its consistency, a reasonable sampling of well characterized steel welds (i.e., 8 different welds) are considered, for which solidification and estimated HAZ-edge boundaries where determined experimentally [36].

The organization of the subject areas presented are as follows. First, a brief description of the general procedure for inverse analysis of heat deposition processes is presented. Second, results of inverse thermal analyses of structural steel deep penetration welds are presented. These results provide a quantitative parametric representation of temperature histories for these welds and for any welds associated with similar welding process conditions. Third, a discussion is presented of the results and of using experimentally measured HAZ edges for a consistency check of calculated temperature histories. Finally, a conclusion is given.

Inverse Analysis Procedure

Following the inverse analysis approach, a parametric model provides a means for the inclusion of information concerning the physical characteristics of a given energy deposition process. A physically consistent parametric representation of temperature fields for heat deposition during welding of plate structures is given by

$$T(\hat{x},t) = T_A + \sum_{k=1}^{N_k}\sum_{n=1}^{N_t} C(\hat{x}_k) G(\hat{x},\hat{x}_k,\kappa,n\Delta t,V) \qquad \text{(Eq 1)}$$

and

$$T(\hat{x}_n^c, t_n^c) = T_n^c\,, \qquad \text{(Eq 2)}$$

where

$$G(\hat{x},\hat{x}_k,t,\kappa,V) = \frac{1}{t}\exp\left[-\frac{(x-x_k-Vt)^2+(y-y_k)^2}{4\kappa t}\right] \times\left\{1+2\sum_{m=1}^{\infty}\exp\left[-\frac{\kappa m^2\pi^2 t}{l^2}\right]\cos\left[\frac{m\pi z}{l}\right]\cos\left[\frac{m\pi z_k}{l}\right]\right\}, \qquad \text{(Eq 3)}$$

and

$$C(\hat{x}) = \sum_{k=1}^{N_k} Q(\hat{x}_k)\delta(\hat{x}-\hat{x}_k)\,. \qquad \text{(Eq 4)}$$

where $Q(\hat{x}_k)$ is the value of the discrete source function at location $\hat{x}_k$. The quantities κ, V and l are the thermal diffusivity, welding speed and plate thickness, respectively. The constraint conditions defined by Eq.(2), which represent input for the model defined by Eqs.(1)-(4), are imposed on the temperature field by minimization of the objective function defined by

$$Z_T = \sum_{n=1}^{N} w_n \left(T(\hat{x}_n^c, t_n^c) - T_n^c \right)^2 \qquad \text{(Eq 5)}$$

where T_n^c is the target temperature for position $\hat{x}_n^c = (x_n^c, y_n^c, z_n^c)$. The quantities w_n ($n=1,\ldots,N$) are weight coefficients that specify relative levels of influence associated with constraint conditions T_n^c. The output quantity of the model defined by Eqs.(1)-(4) is the three-diemsional temperature field $T(\hat{x}, t)$ spanning the entire volume of the workpiece.

The procedure for inverse thermal analysis defined by Eqs.(1)-(5) entails adjustment of the parameters $C(\hat{x}_k)$, $\hat{x}_k$ and Δt. The parametric model combines numerical integration with optimization of linear combinations of numerical-analytical basis functions, which include fundamental solutions to the heat conduction equation and their Fourier-series representation [21]. In particular, Eq.(1) defines a discrete numerical integration over time, where the time step Δt is specified according to the average energy deposited during the time Δt, for transition of the temperature field to steady state. It should be noted that the formulation of the inverse analysis methodology defined by Eq.(1)-(5) is equipped with a mathematical structure that satisfies all boundary conditions associated with welding of plate structures (see [24-27] for further discussion).

In addition to the parameters defined with respect to Eqs.(1)-(5), the parameteric model applied for inverse analysis includes a length scale parameter l_S, where in general $l_S < l$ defined by Eq.(3), for specification of the spatial scale of the calculated temperature field with respect to which parameters are adjusted. This length scale parameter provides for inclusion of more details of shape features of measured solidification boundaries to be adopted as constraint conditions. Inverse analyses using this parameter are given in reference [27, 37]. However, for the analyses that follow, the two length parameters, i.e., the plate thickness l and the depth l_S of the speciifed region of the temperature field to be calculated, are taken to be the same.

Table 1 Experimentally measured estimates of locations (y_c, z_c) on solidification and HAZ-edge boundaries, which are on transverse cross section of Weld 1.

SOLIDIFICATION BOUNDARY	ESTIMATED HAZ-EDGE
(y_c mm, z_c mm)	*(y_c mm, z_c mm)*
(5.052, 0.2105)	(6.315, 0.2105)
(3.579, 2.105)	(5.684, 2.105)
(2.316, 3.158)	(5.052, 3.158)
(2.316, 4.210)	(4.21, 4.21)
(1.895, 6.315)	(3.579, 6.315)
(1.895, 8.420)	(3.368, 8.42)
(1.684, 10.525)	(3.158, 10.525)
(2.316, 12.0)	(3.789,12.0)

Table 2 Experimentally measured estimates of locations (y_c,z_c) on solidification and HAZ-edge boundaries, which are on transverse cross section of Weld 2.

SOLIDIFICATION BOUNDARY	ESTIMATED HAZ-EDGE
(y_c mm, z_c mm)	*(y_c mm, z_c mm)*
(7.578, 0.2105)	(9.262, 0.2105)
(5.894, 1.053)	(8.42, 1.053)
(4.421, 2.105)	(7.578, 2.105)
(3.158, 3.158)	(6.736, 3.158)
(2.316, 4.21)	(5.473, 4.21)
(2.105, 5.263)	(4.421, 5.263)
(1.684, 7.368)	(3.368, 7.368)
(1.684, 9.473)	(3.158, 9.473)
(1.474, 10.525)	(3.158, 10.525)
(2.105, 12.0)	(3.579, 12.0)

Table 3 Experimentally measured estimates of locations (y_c,z_c) on solidification and HAZ-edge boundaries, which are on transverse cross section of Weld 3.

SOLIDIFICATION BOUNDARY	ESTIMATED HAZ-EDGE
(y_c mm, z_c mm)	*(y_c mm, z_c mm)*
(5.164, 0.2459)	(7.377, 0.2459)
(3.934, 2.459)	(6.393, 2.459)
(1.967, 4.918)	(4.918, 4.918)
(2.213, 7.377)	(3.443, 7.377)
(1.721, 9.836)	(3.197, 9.836)
(1.721, 12.30)	(2.705, 12.30)
(1.475, 14.75)	(2.705, 14.75)

Table 4 Experimentally measured estimates of locations (y_c,z_c) of solidification and HAZ-edge boundaries, which are on transverse cross section of Weld 4.

SOLIDIFICATION BOUNDARY	ESTIMATED HAZ-EDGE
(y_c mm, z_c mm)	*(y_c mm, z_c mm)*
(5.090, 0.2679)	(7.501, 0.2679)
(5.090, 1.340)	(6.965, 1.340)
(4.019, 2.679)	(6.430, 2.679)
(2.947, 4.019)	(5.626, 4.019)
(1.875, 5.358)	(4.822, 5.358)
(1.875, 8.037)	(3.483, 8.037)
(1.607, 10.72)	(2.947, 10.72)
(1.875, 12.06)	(2.947, 12.06)
(1.607, 13.40)	(2.679, 13.40)
(1.607, 14.73)	(2.679, 14.73)

Table 5 Experimentally measured estimates of locations (y_c,z_c) on solidification and HAZ-edge boundaries, which are on transverse cross section of Weld 5.

SOLIDIFICATION BOUNDARY	ESTIMATED HAZ-EDGE
(y_c mm, z_c mm)	*(y_c mm, z_c mm)*
(7.501, 0.2679)	(10.18, 0.2679)
(6.965, 1.340)	(9.912, 1.340)
(5.894, 2.679)	(9.644, 2.679)
(4.554, 4.019)	(8.573, 4.019)
(2.947, 5.358)	(7.501, 5.358)
(2.411, 6.698)	(5.894, 6.698)
(2.411, 8.037)	(4.554, 8.037)
(2.143, 9.377)	(4.019, 9.377)
(2.143, 10.72)	(3.751, 10.72)
(1.875, 13.40)	(3.483, 13.40)
(1.875, 14.73)	(3.483, 14.73)

Table 6 Experimentally measured estimates of locations (y_c,z_c) on solidification and HAZ-edge boundaries, which are on transverse cross section of Weld 6.

SOLIDIFICATION BOUNDARY	ESTIMATED HAZ-EDGE
(y_c mm, z_c mm)	*(y_c mm, z_c mm)*
(8.773, 0.2830)	(10.47, 0.2830)
(8.207, 1.415)	(10.47, 1.415)
(6.792, 2.830)	(9.905, 2.830)
(5.377, 4.019)	(9.056, 4.019)
(3.679, 5.66)	(7.924, 5.66)
(2.264, 7.075)	(6.509, 7.075)
(2.264, 8.037)	(5.094, 8.037)
(1.981, 11.32)	(3.962, 11.32)
(1.981, 12.74)	(3.962, 12.74)
(2.264, 14.15)	(3.962, 14.15)
(2.264, 15.0)	(3.962, 15.0)

Table 7 Experimentally measured estimates of locations (y_c,z_c) on solidification and HAZ-edge boundaries, which are on transverse cross section of Weld 7.

SOLIDIFICATION BOUNDARY	ESTIMATED HAZ-EDGE
(y_c mm, z_c mm)	*(y_c mm, z_c mm)*
(9.793, 0.3159)	(12.32, 0.3159)
(8.529, 1.580)	(11.69, 1.580)
(6.634, 3.159)	(10.11, 3.159)
(4.739, 4.739)	(8.845, 4.739)
(3.159, 6.318)	(6.95, 6.318)
(2.211, 7.898)	(5.686, 7.898)
(2.843, 9.477)	(4.423, 9.477)
(2.843, 11.06)	(4.107, 11.06)
(2.211, 12.64)	(3.475, 12.64)
(1.589, 14.22)	(3.159, 14.22)
(2.211, 15.80)	(3.475, 15.80)
(2.527, 17.37)	(3.791, 17.37)
(2.211, 18.0)	(3.791, 18.0)

Table 8 Experimentally measured estimates of locations (y_c,z_c) on solidification and HAZ-edge boundaries, which are on transverse cross section of Weld 8.

SOLIDIFICATION BOUNDARY	ESTIMATED HAZ-EDGE
(y_c mm, z_c mm)	*(y_c mm, z_c mm)*
(7.938, 0.3175)	(12.38, 0.3175)
(7.62, 3.175)	(12.38, 3.175)
(6.668, 4.763)	(11.75, 4.763)
(5.398, 6.35)	(10.80, 6.35)
(4.128, 7.938)	(9.842, 7.938)
(3.81, 9.525)	(8.255, 9.525)
(2.858, 12.7)	(6.35, 12.7)
(2.54, 15.89)	(5.398, 15.89)
(3.175, 19.05)	(5.715, 19.05)
(2.858, 20.0)	(6.033, 20.0)

Case Study Analysis of Steel Welds

In this section results of inverse thermal analyses of structural steel deep-penetration welds are described, which correspond to different weld process conditions and associated process-control parameters. The significance of the inverse-problem approach for these analyses is that the nature of the coupling of the energy source to the workpiece, which is a function of beam power and process control parameters, is in principle difficult to specify relative to analysis based on the direct-problem approach. Previous studies considered inverse thermal analysis of steel welds using different types of constraint conditions [25,26]. The present study uses experimentally estimated solidification boundaries for assigning volumetric constraints (see Eq.(2)) on the calculated temperature fields. As discussed in reference [27], for regions within the workpiece not close to the energy source, reasonable estimates of temprature-field values, at specified locations, are sufficient for imposing constraint conditions.

For steel welds, especially those of structural steel, the HAZ consists by various regions whose microstructures have been well characterized (see reference [1]). These regions are described schematically in Fig. 1. Referring to this figure, it should be noted that, for inverse thermal analysis of structural steel welds, one should be able to associate the observed edge of the HAZ with a range of temperatures characteristic of that region of the weld (see Fig. 1).

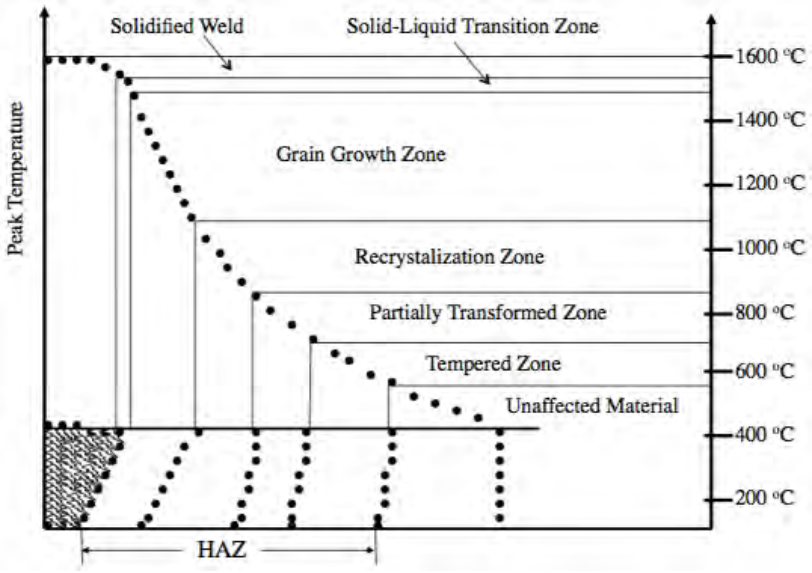

Fig. 1 Schematic representation of different regions within the HAZ for steel welds and approximate location of experimentally observable HAZ edge.

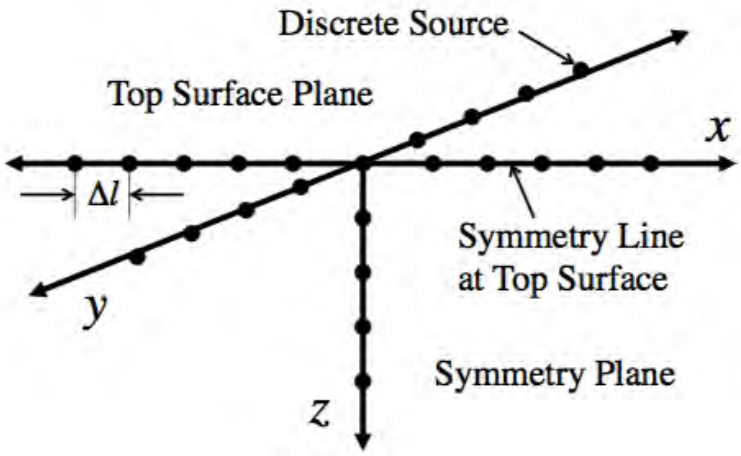

Fig. 2 Indexing scheme for relative locations of discrete sources $C(\hat{x}_k)$, $k=1,...,N_k$.

The structural steel deep-penetration welds, whose inverse analysis is presented here, consist of laser and laser-GMA hybrid welds [38]. The analyses presented here entail calculation of the steady state temperature field for a specified range of sizes and shapes of inner surface boundaries defined by the solidification boundary, and experimentally observed estimates of the HAZ edge. The shapes of these boundaries are determined experimentally by analysis of transverse weld cross sections showing microstructure revealing solidification and estimated HAZ-edge boundaries. For calculations of the temperature field, which adopt solidification boundaries as constraints, the parameter values assumed are $\kappa = 5.88 \times 10^{-6}$ m^2s^{-1}, $T_M = 1503.0$ ^oC. As discussed previously [25, 27], reasonable estimates of κ and T_M are sufficient for inverse analysis. This assumption is sufficient, within reasonable estimates, in that the set of parameters $C(\hat{x}_k)$, $k=1,...,N_k$, and κ are not uniquely determined by inverse analysis. Thus, changing estimated values of κ would require different values of $C(\hat{x}_k)$ in order to satisfy specified constraint conditions associated with T_M. With respect to inverse analysis, the interpretation of κ as both an estimated material property and adjustable parameter is emphasized within the following.

The goal of the present analysis is determination of a set of parameters that can serve as initial estimates for parameter adjustment with respect to deep penetration welds of steels, whose process parameters are within similar regimes. Parameter adjustment with respect to other welds, which assume the results of this study as initial estimates, would adopt κ and T_M as adjustable parameters, as well as the discrete source function $C(\hat{x}_k)$. Values of the workpiece thickness l and welding speed V defined in Eq. (3) are given in the figures below. The upstream boundary constraints on the temperature field, $T_c = T_M$ for (y_c,z_c) defined in Eq. (2), are given in Tables 1 through 8 for the solidification boundaries. Given in Tables 9 through 16 are values of the discrete source function that have been calculated according to the constraint conditions and weld specifications given in Tables 1 through 8. The relative location of each discrete source is specified according to indexing scheme shown in Fig. 2. Shown in Figs. 3 through 42 are experimentally measured transverse weld cross sections of solidification and estimated HAZ-edge boundaries [38], and different planer slices of the steady state temperature field that have been calculated according to the constraint conditions given in Tables 1 through 8 for the solidification boundary. Referring to the planar slices of the

calculated temperature fields shown in these figures, it can be seen that all boundary conditions are satisfied, namely the condition $T(\hat{x},t) = T_M$ at the solidification boundary, and $\nabla T \cdot \hat{n} = 0$ at surface boundaries, where $\hat{n}$ is normal to the surface.

Table 9 Source function $C(\hat{x}_k)$ calculated according to solidification-boundary constraint conditions given in Table 1, where Δl = (12/60) mm, $x_k = y_k = 0.0$ for k = 1 to 13 (WELD 1).

k	C_k/20.0	z_k (Δl)
1	0.23	1
2	0.10	5
3	0.10	10
4	0.07	15
5	0.07	20
6	0.07	25
7	0.07	30
8	0.07	35
9	0.065	40
10	0.065	45
11	0.06	50
12	0.05	55
13	0.05	60

Table 10 Source function $C(\hat{x}_k)$ calculated according to solidification-boundary constraint conditions given in Table 2, where Δl = (12/60) mm, $x_k = y_k = 0.0$ for k = 1 to 13 and z_k = 1 for k = 14 to 17 (WELD 2).

k	C_k/11.5	z_k (Δl)
1	0.10	1
2	0.10	5
3	0.10	10
4	0.10	15
5	0.10	20
6	0.10	25
7	0.10	30
8	0.10	35
9	0.10	40
10	0.10	45
11	0.10	50
12	0.06	55
13	0.09	60

k	C_k	x_k (Δl)	y_k (Δl)
14	2.4	-10.0	0.0
15	2.4	10.0	0.0
16	2.4	0.0	-10.0
17	2.4	0.0	10.0

Table 11 Source function $C(\hat{x}_k)$ calculated according to solidification-boundary constraint conditions given in Table 3, where Δl = (15/60) mm, $x_k = y_k = 0.0$ for k = 1 to 13 (WELD 3).

k	C_k/15.5	z_k (Δl)
1	0.40	1
2	0.10	5
3	0.10	10
4	0.10	15
5	0.10	20
6	0.10	25
7	0.10	30
8	0.10	35
9	0.10	40
10	0.10	45
11	0.08	50
12	0.07	55
13	0.04	60

Table 12 Source function $C(\hat{x}_k)$ calculated according to solidification-boundary constraint conditions given in Table 4, where Δl = (15/60) mm, $x_k = y_k = 0.0$ for k = 1 to 13 (WELD 4).

k	C_k/15.5	z_k (Δl)
1	0.40	1
2	0.10	5
3	0.10	10
4	0.10	15
5	0.10	20
6	0.10	25
7	0.10	30
8	0.10	35
9	0.10	40
10	0.10	45
11	0.08	50
12	0.08	55
13	0.05	60

Table 13 Source function $C(\hat{x}_k)$ calculated according to solidification-boundary constraint conditions given in Table 5, where Δl = (15/60) mm, $x_k = y_k = 0.0$ for k = 1 to 13 (WELD 5).

k	C_k/17.5	z_k (Δl)
1	0.40	1
2	0.30	5
3	0.30	10
4	0.10	15
5	0.10	20
6	0.10	25
7	0.10	30
8	0.10	35
9	0.10	40
10	0.10	45
11	0.09	50
12	0.09	55
13	0.05	60

Table 14 Source function $C(\hat{x}_k)$ calculated according to solidification-boundary constraint conditions given in Table 6, where Δl = (3.0/60) mm, $x_k = y_k = 0.0$ for k = 1 to 13 (WELD 6).

k	C_k/17.5	z_k (Δl)
1	0.80	1
2	0.30	5
3	0.30	10
4	0.10	15
5	0.10	20
6	0.10	25
7	0.10	30
8	0.10	35
9	0.10	40
10	0.10	45
11	0.09	50
12	0.09	55
13	0.05	60

Table 15 Source function $C(\hat{x}_k)$ calculated according to solidification-boundary constraint conditions given in Table 7, where Δl = (18/60) mm, $x_k = y_k = 0.0$ for k = 1 to 13 (WELD 7).

k	C_k/17.5	z_k (Δl)
1	1.00	1
2	0.30	5
3	0.20	10
4	0.10	15
5	0.10	20
6	0.15	25
7	0.15	30
8	0.20	35
9	0.10	40
10	0.10	45
11	0.12	50
12	0.15	55
13	0.05	60

Table 16 Source function $C(\hat{x}_k)$ calculated according to solidification-boundary constraint conditions given in Table 8, where Δl = (20/60) mm, $x_k = y_k = 0.0$ for k = 1 to 13 (WELD 8).

k	C_k/25.0	z_k (Δl)
1	0.40	1
2	0.38	5
3	0.35	10
4	0.15	15
5	0.15	20
6	0.15	25
7	0.15	30
8	0.14	35
9	0.12	40
10	0.12	45
11	0.12	50
12	0.12	55
13	0.09	60

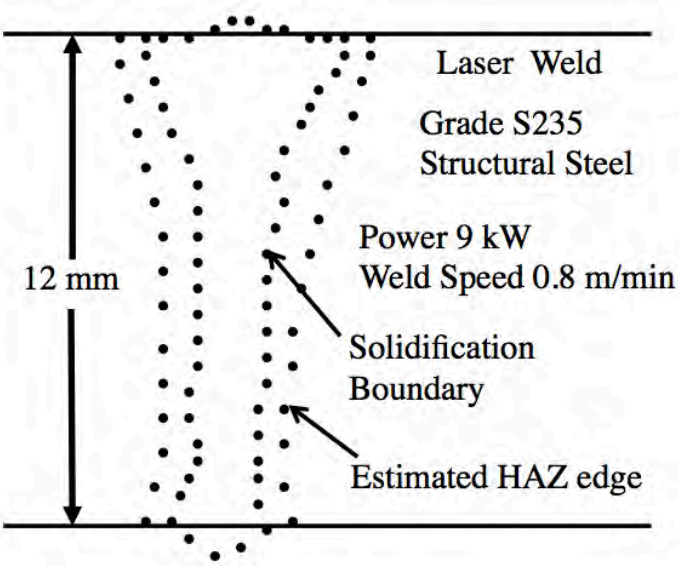

Fig. 3 Experimentally measured transverse weld cross sections of solidification and HAZ-edge boundaries for steel laser weld (Weld 1).

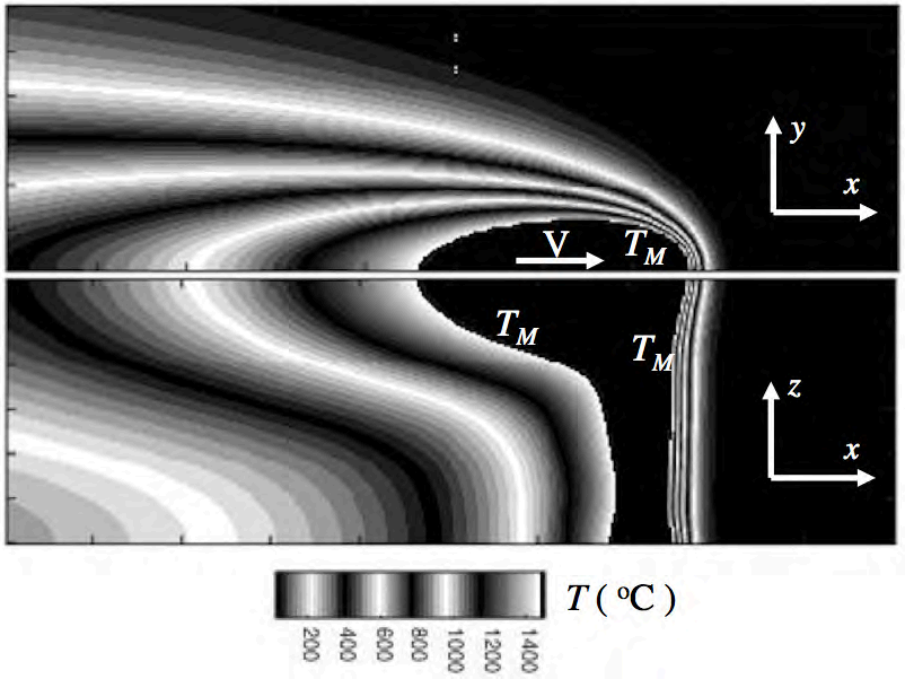

Fig. 4 Two-dimensional slices, at half workpiece top surface and longitudinal cross section at symmetry plane, of three-dimensional temperature field (^{o}C) calculated using cross section information given in Table 1 for solidification boundary (Weld 1).

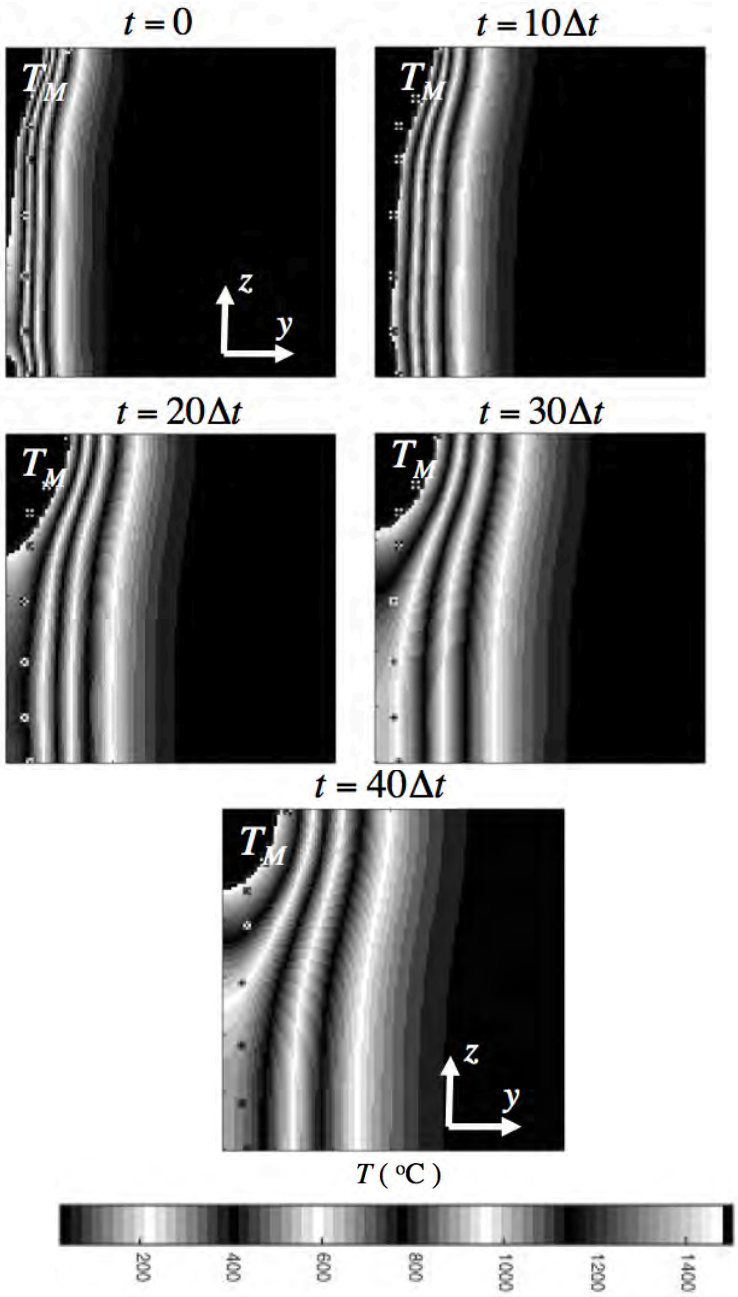

Fig. 5 Temperature history (^{o}C) of transverse cross section of weld calculated using cross section information given in Table 1 for solidification boundary, where $\Delta t = \Delta l$ /V, Δl = (12/60) mm and V = 0.8 m/min (Weld 1).

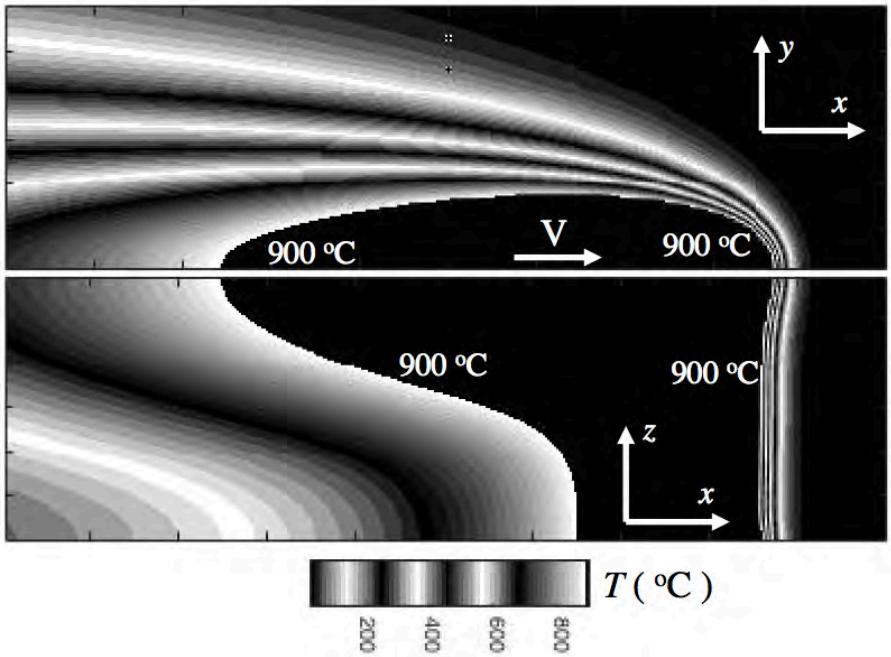

Fig. 6 Two-dimensional slices, at half workpiece top surface and longitudinal cross section at symmetry plane, of three-dimensional temperature field (^{o}C) at estimated HAZ-edge boundary calculated using constraints defined by Eq.(2), and given in Table 1 for solidification boundary (Weld 1).

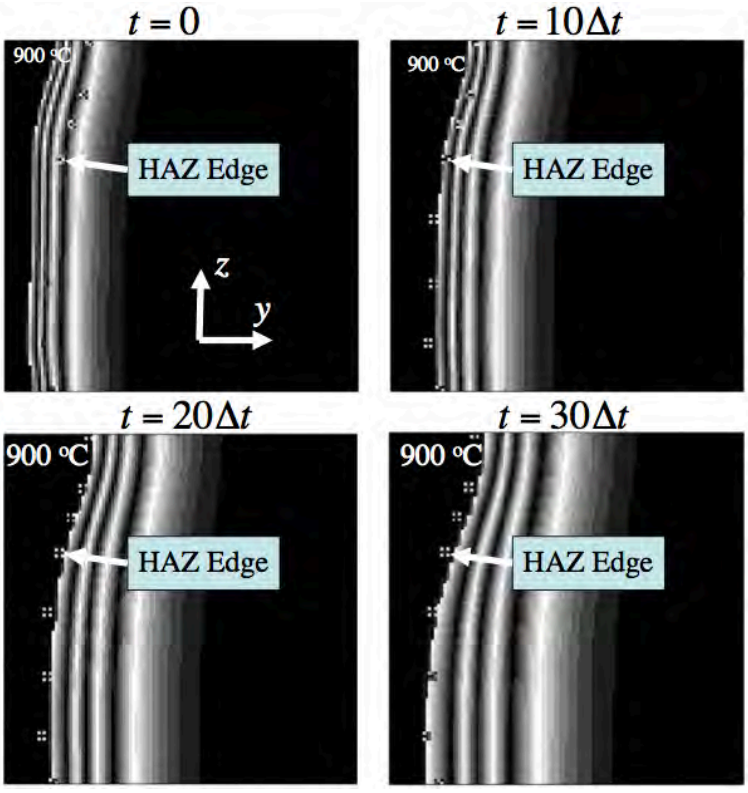

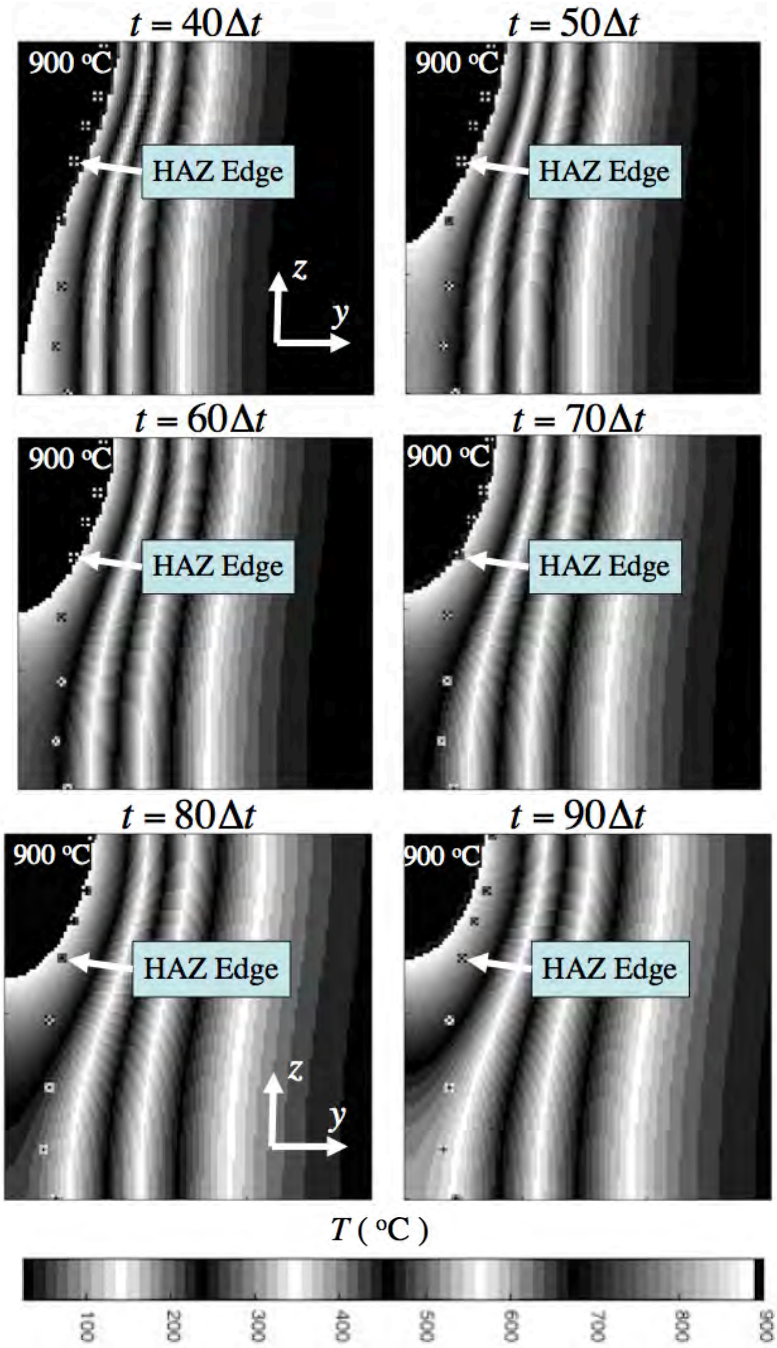

Fig. 7 Temperature history (^{o}C) at estimated HAZ-edge boundary of transverse cross section of weld calculated using constraints defined by Eq.(2), and given in Table 1 for solidification boundary, where $\Delta t = \Delta l$ /V, Δl = (12/60) mm and V = 0.8 m/min (Weld 1).

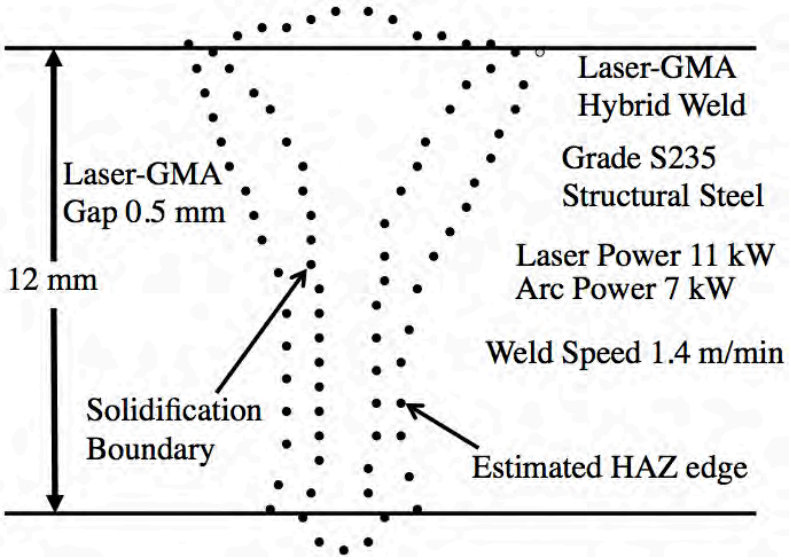

Fig. 8 Experimentally measured transverse weld cross sections of solidification and HAZ-edge boundaries for steel laser-GMA hybrid weld (Weld 2).

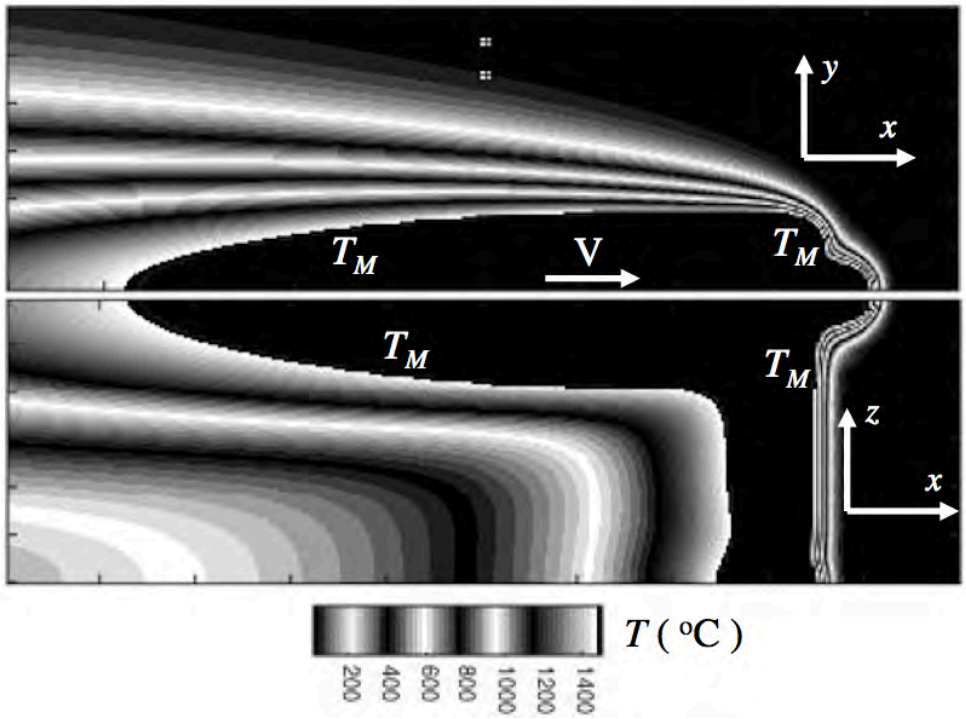

Fig. 9 Two-dimensional slices, at half workpiece top surface and longitudinal cross section at symmetry plane, of three-dimensional temperature field (^{o}C) calculated using cross section information given in Table 2 for solidification boundary (Weld 2).

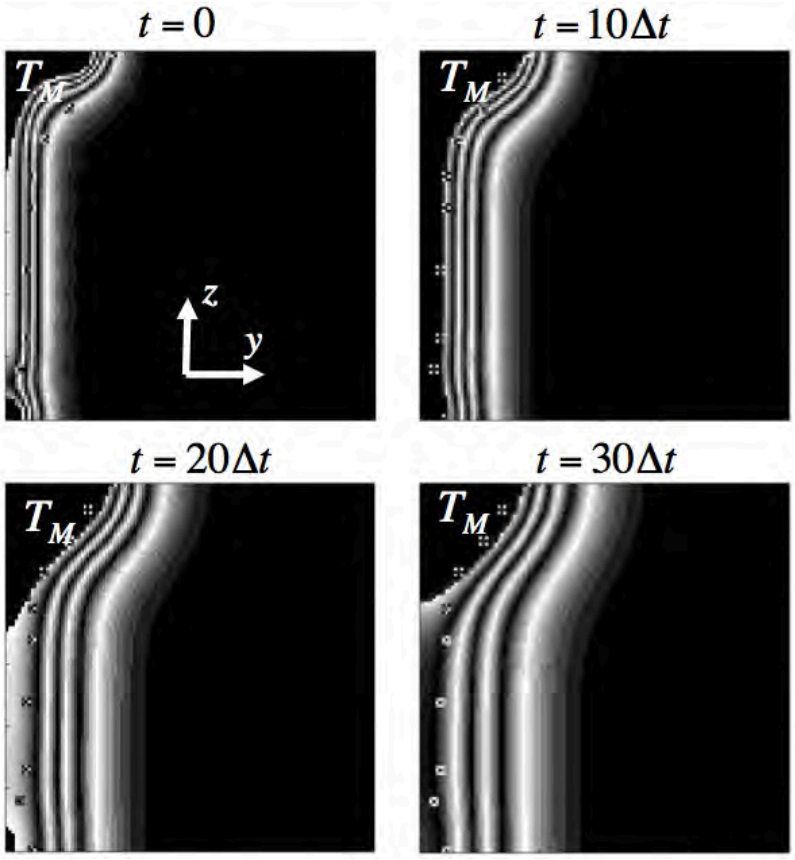
$t = 0$
$t = 10\Delta t$
$t = 20\Delta t$
$t = 30\Delta t$
T_M
z
y

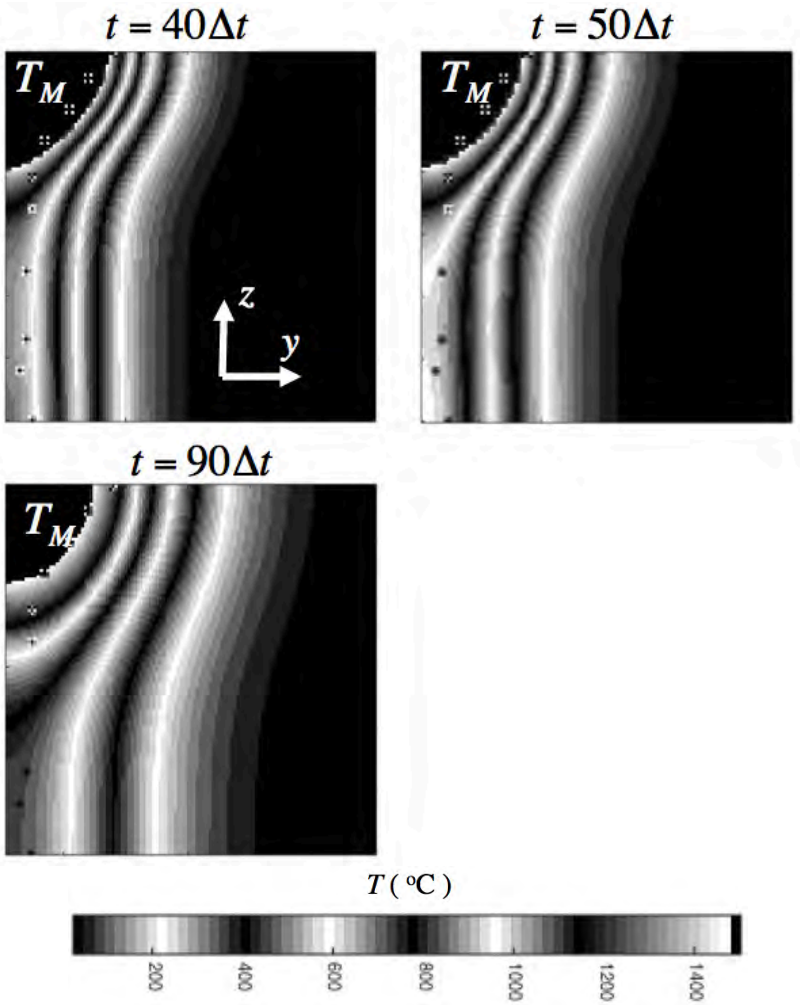

Fig. 10 Temperature history (^{o}C) of transverse cross section of weld calculated using cross section information given in Table 2 for solidification boundary, where $\Delta t = \Delta l$ /V, Δl = (12/60) mm and V = 1.4 m/min (Weld 2).

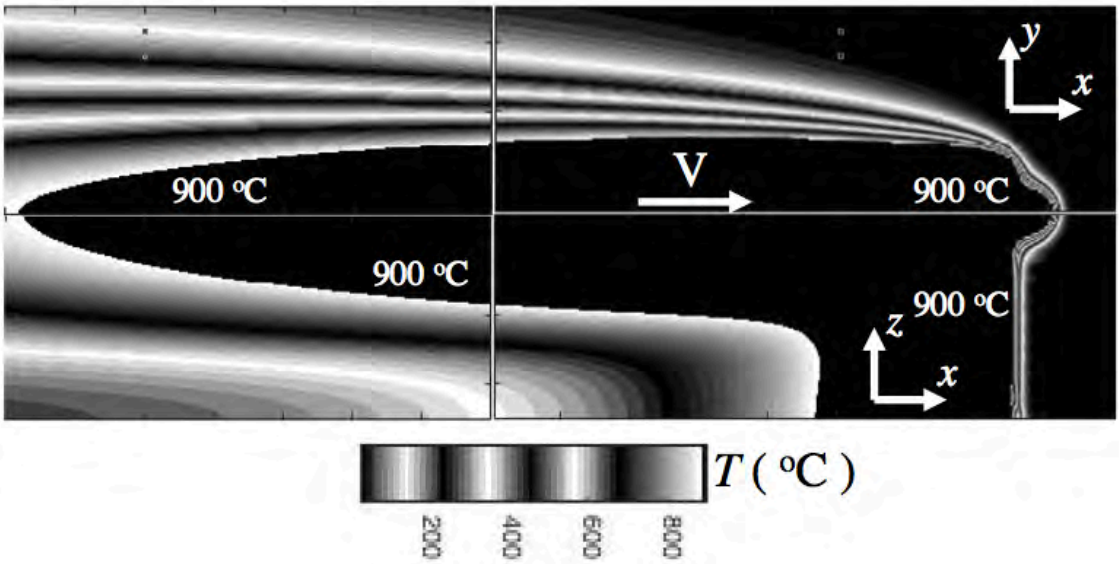

Fig. 11 Two-dimensional slices, at half workpiece top surface and longitudinal cross section at symmetry plane, of three-dimensional temperature field (^{o}C) at estimated HAZ-edge boundary calculated using constraints defined by Eq.(2), and given in Table 2 for solidification boundary (Weld 2).

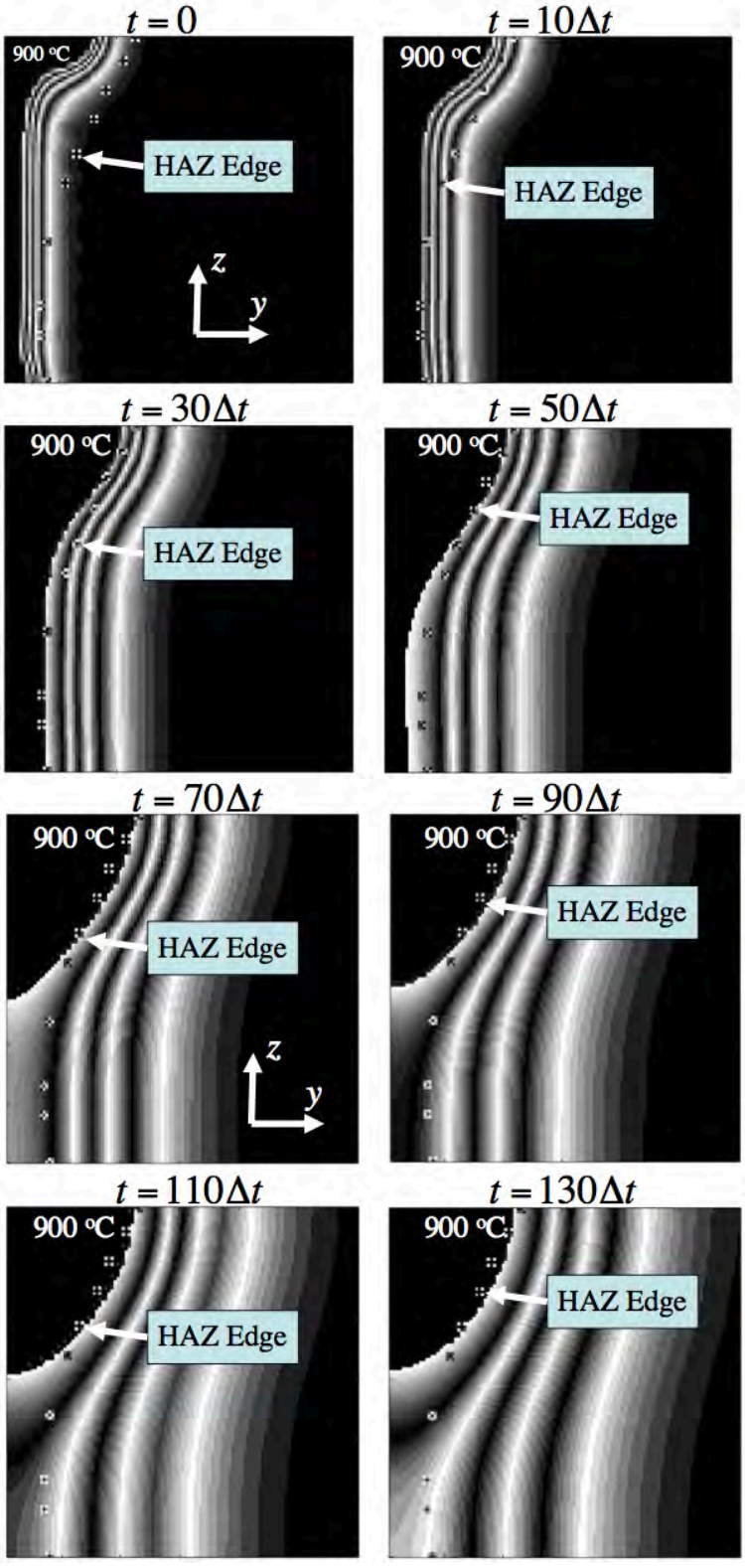
t = 0
900 °C
HAZ Edge
z
y
t = 10Δt
900 °C
HAZ Edge
t = 30Δt
900 °C
HAZ Edge
t = 50Δt
900 °C
HAZ Edge
t = 70Δt
900 °C
HAZ Edge
z
y
t = 90Δt
900 °C
HAZ Edge
t = 110Δt
900 °C
HAZ Edge
t = 130Δt
900 °C
HAZ Edge

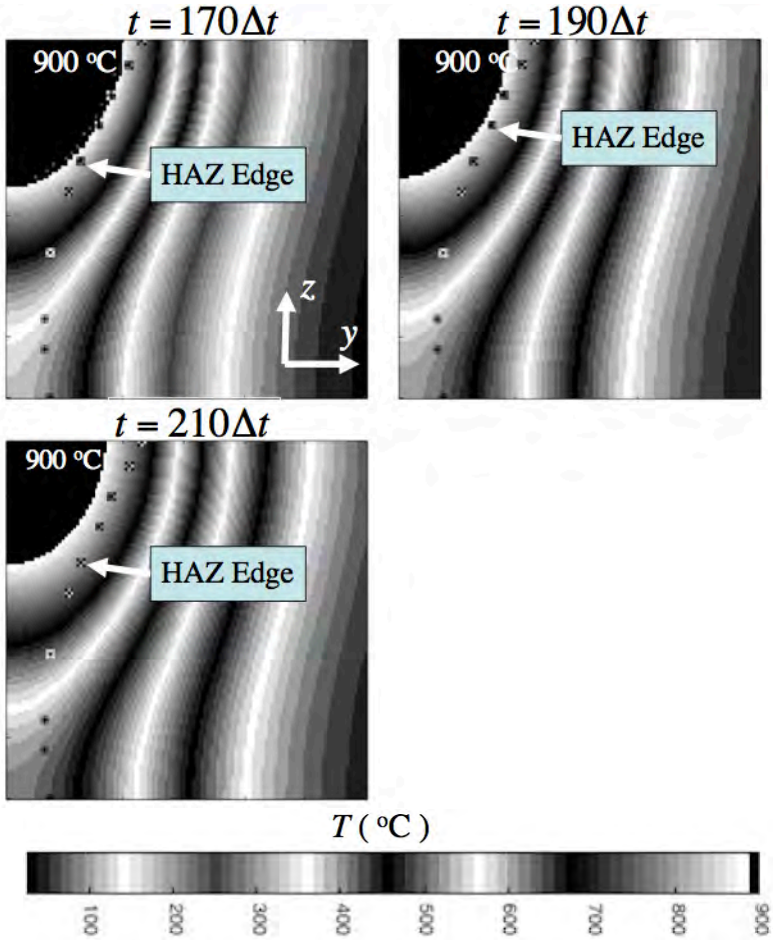

Fig. 12 Temperature history (^{o}C) at estimated HAZ-edge boundary of transverse cross section of weld calculated using constraints defined by Eq.(2), and given in Table 2 for solidification boundary, where $\Delta t = \Delta l$ /V, Δl = (12/60) mm and V = 1.4 m/min (Weld 2).

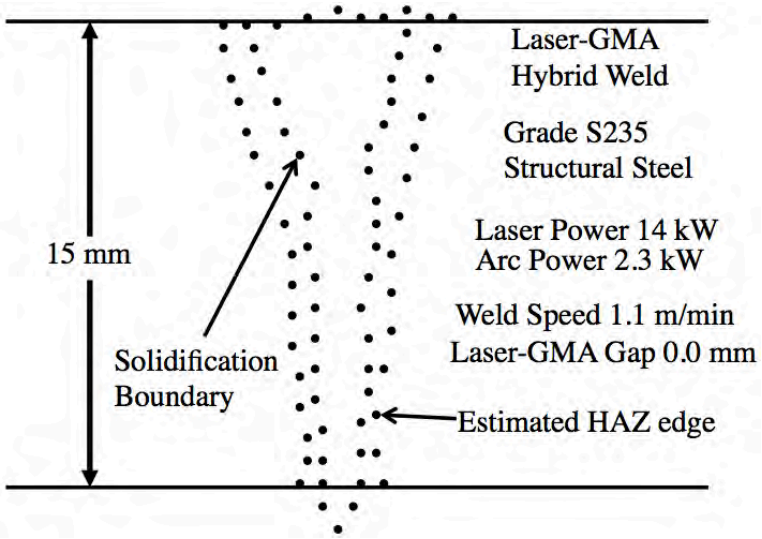

Fig. 13 Experimentally measured transverse weld cross sections of solidification and HAZ-edge boundaries for steel laser-GMA hybrid weld (Weld 3).

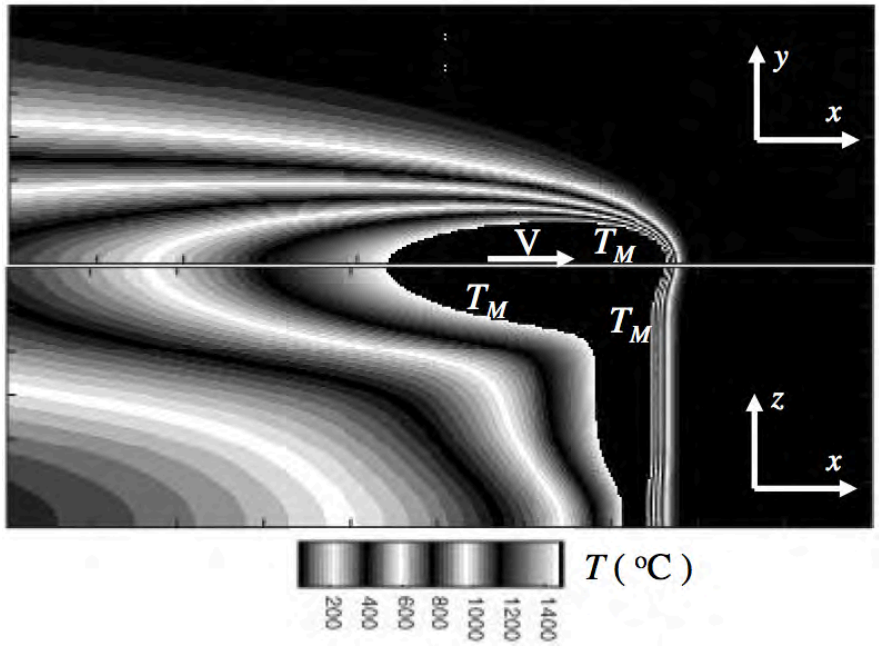

Fig. 14 Two-dimensional slices, at half workpiece top surface and longitudinal cross section at symmetry plane, of three-dimensional temperature field (^{o}C) calculated using cross section information given in Table 3 for solidification boundary (Weld 3).

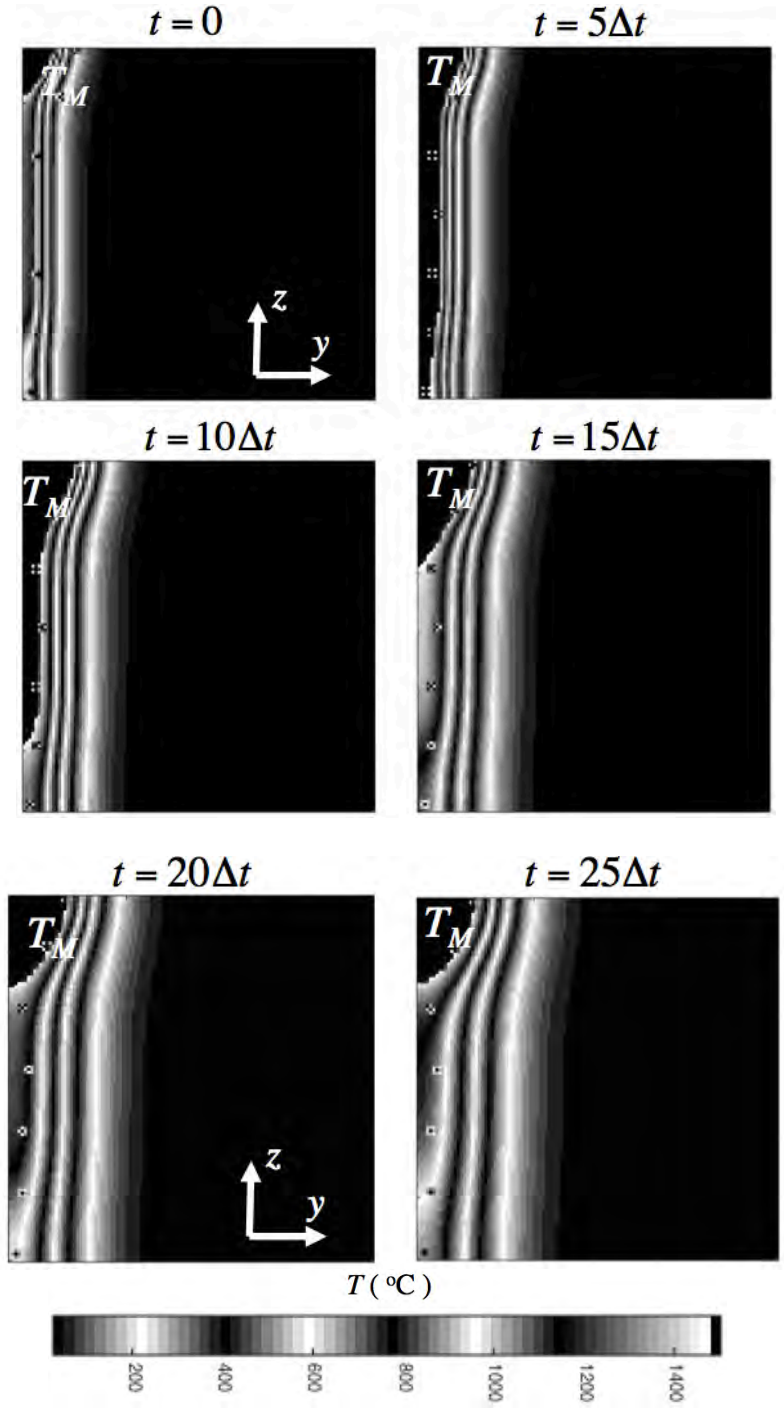

Fig. 15 Temperature history (^{o}C) of transverse cross section of weld calculated using cross section information given in Table 3 for solidification boundary, where $\Delta t = \Delta l$ /V, Δl = (15/60) mm and V = 1.1 m/min (Weld 3).

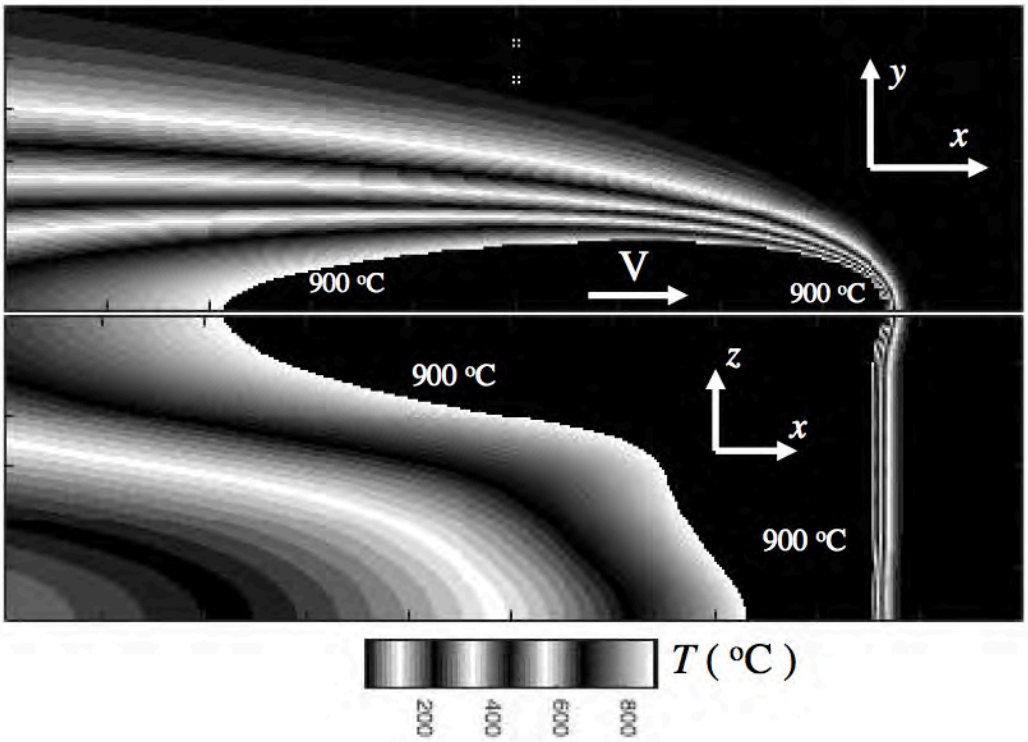

Fig. 16 Two-dimensional slices, at half workpiece top surface and longitudinal cross section at symmetry plane, of three-dimensional temperature field (^{o}C) at estimated HAZ-edge boundary calculated using constraints defined by Eq.(2), and given in Table 3 for solidification boundary (Weld 3).

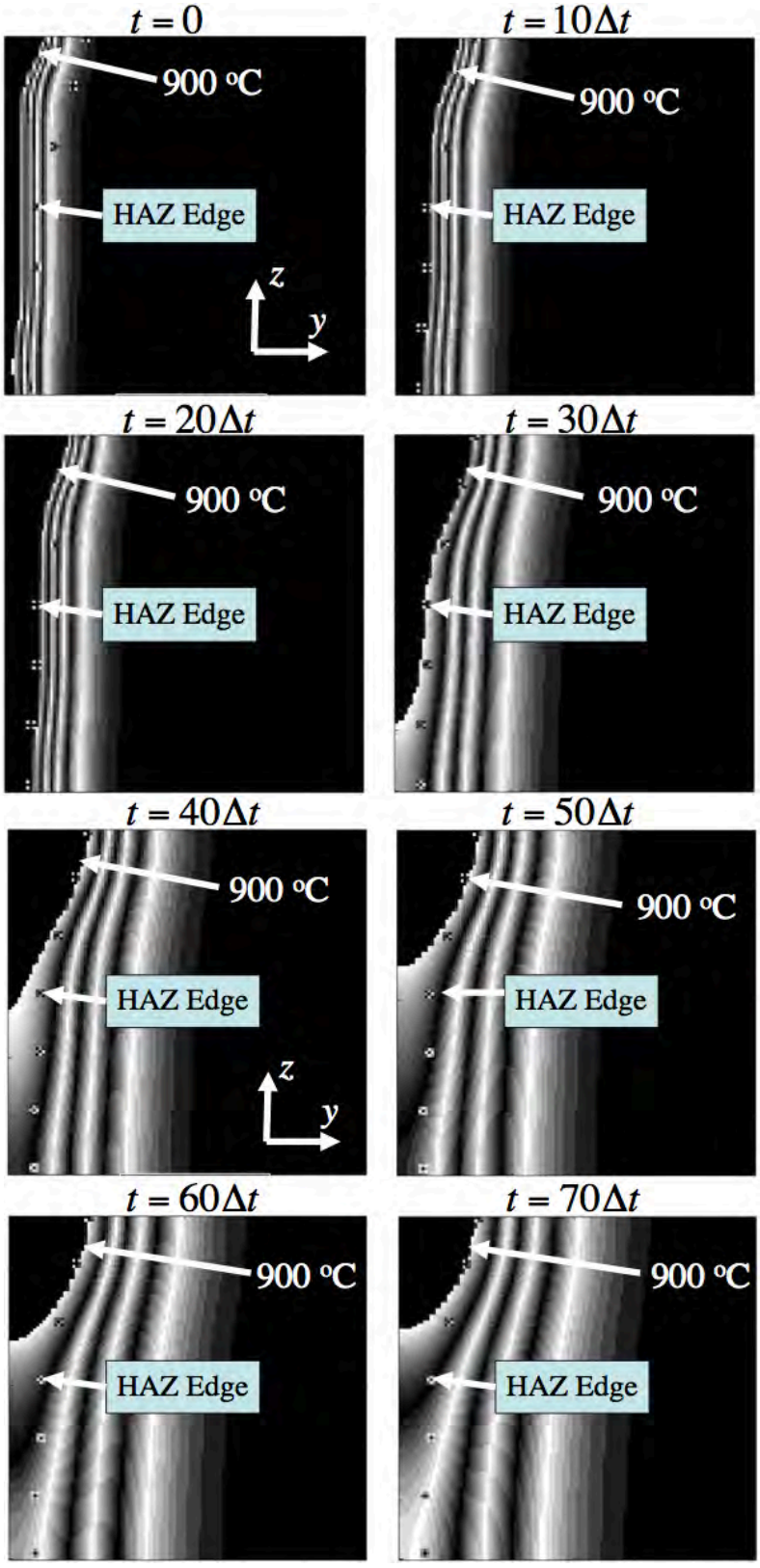
t = 0
900 °C
HAZ Edge
z
y
t = 10Δt
900 °C
HAZ Edge
t = 20Δt
900 °C
HAZ Edge
t = 30Δt
900 °C
HAZ Edge
t = 40Δt
900 °C
HAZ Edge
z
y
t = 50Δt
900 °C
HAZ Edge
t = 60Δt
900 °C
HAZ Edge
t = 70Δt
900 °C
HAZ Edge

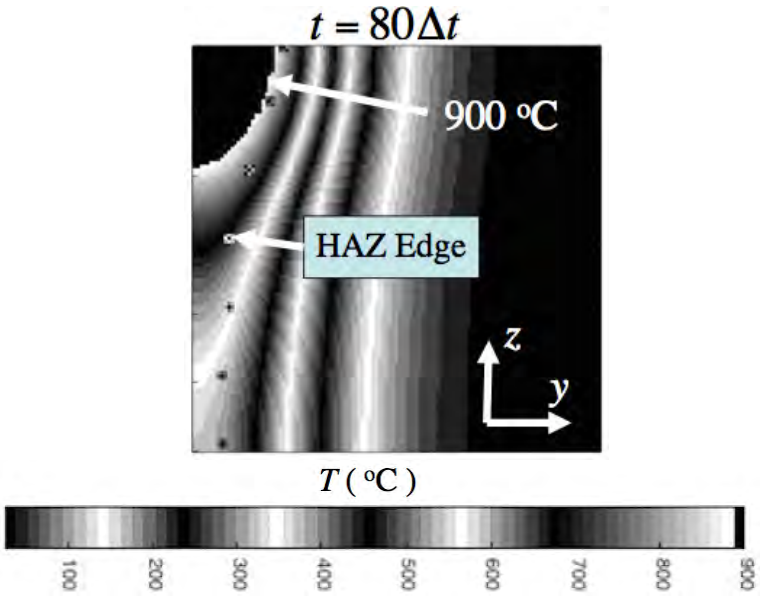

Fig. 17 Temperature history (^{o}C) at estimated HAZ-edge boundary of transverse cross section of weld calculated using constraints defined by Eq.(2), and given in Table 3 for solidification boundary, where $\Delta t = \Delta l$ /V, Δl = (15/60) mm and V = 1.1 m/min (Weld 3).

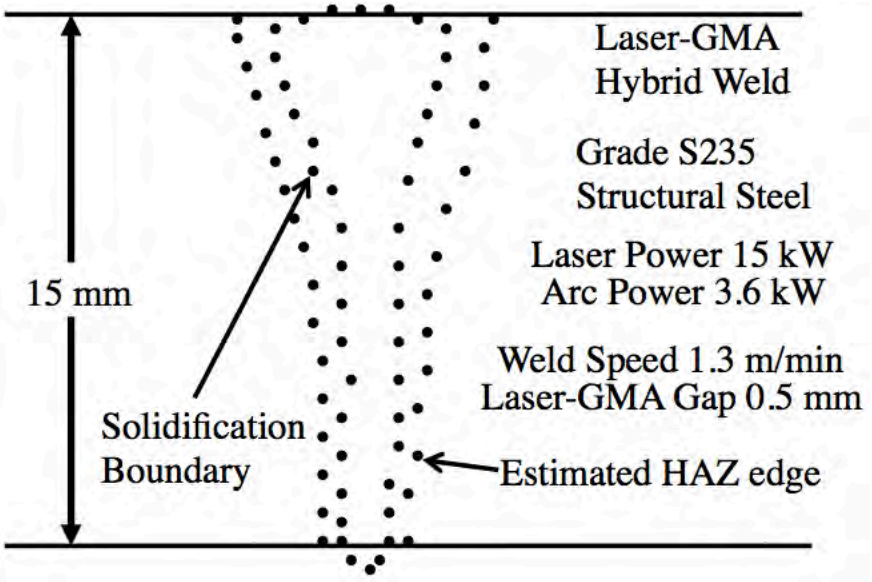

Fig. 18 Experimentally measured transverse weld cross sections of solidification and HAZ-edge boundaries for steel laser-GMA hybrid weld (Weld 4).

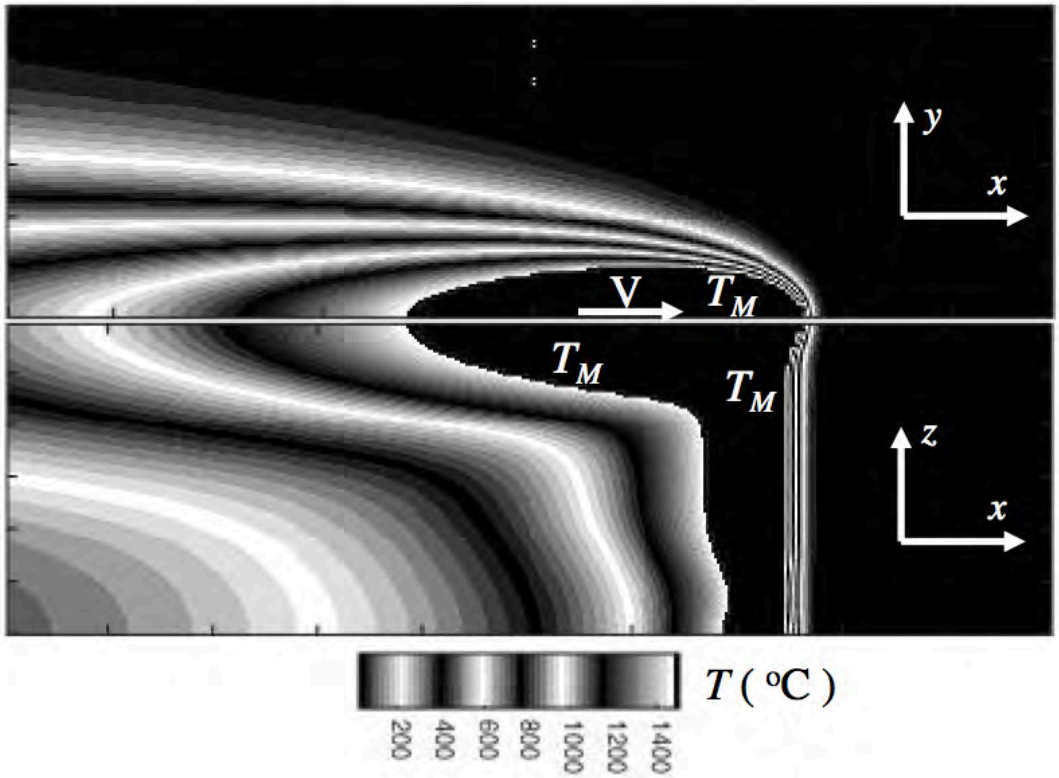

Fig. 19 Two-dimensional slices, at half workpiece top surface and longitudinal cross section at symmetry plane, of three-dimensional temperature field (^{o}C) calculated using cross section information given in Table 4 for solidification boundary (Weld 4).

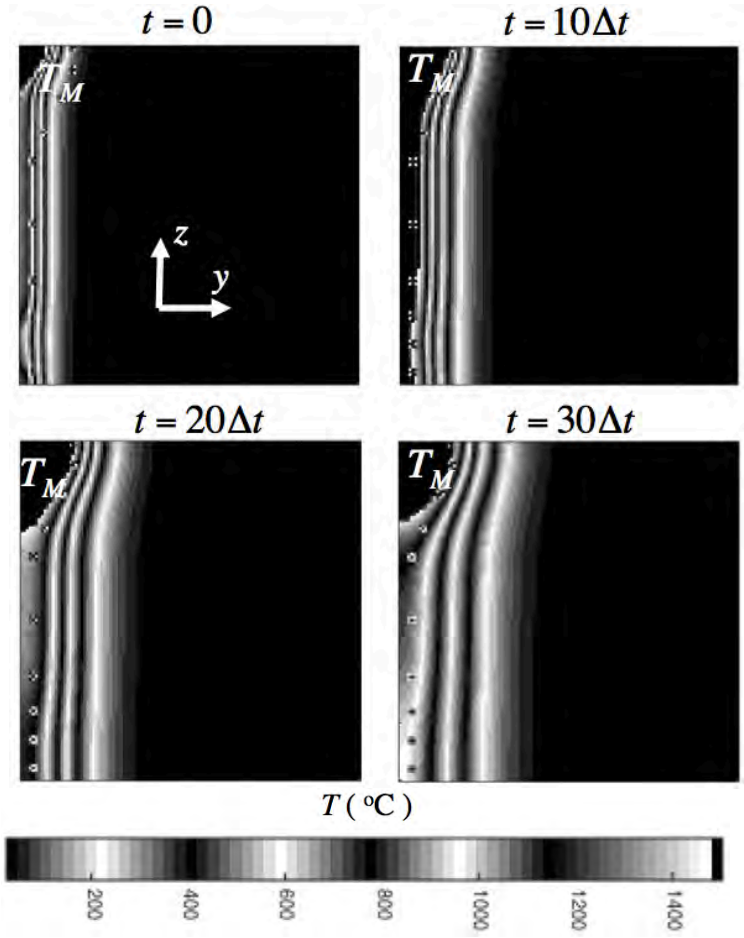

Fig. 20 Temperature history (^{o}C) of transverse cross section of weld calculated using cross section information given in Table 4 for solidification boundary, where $\Delta t = \Delta l$ /V, Δl = (15/60) mm and V = 1.3 m/min (Weld 4).

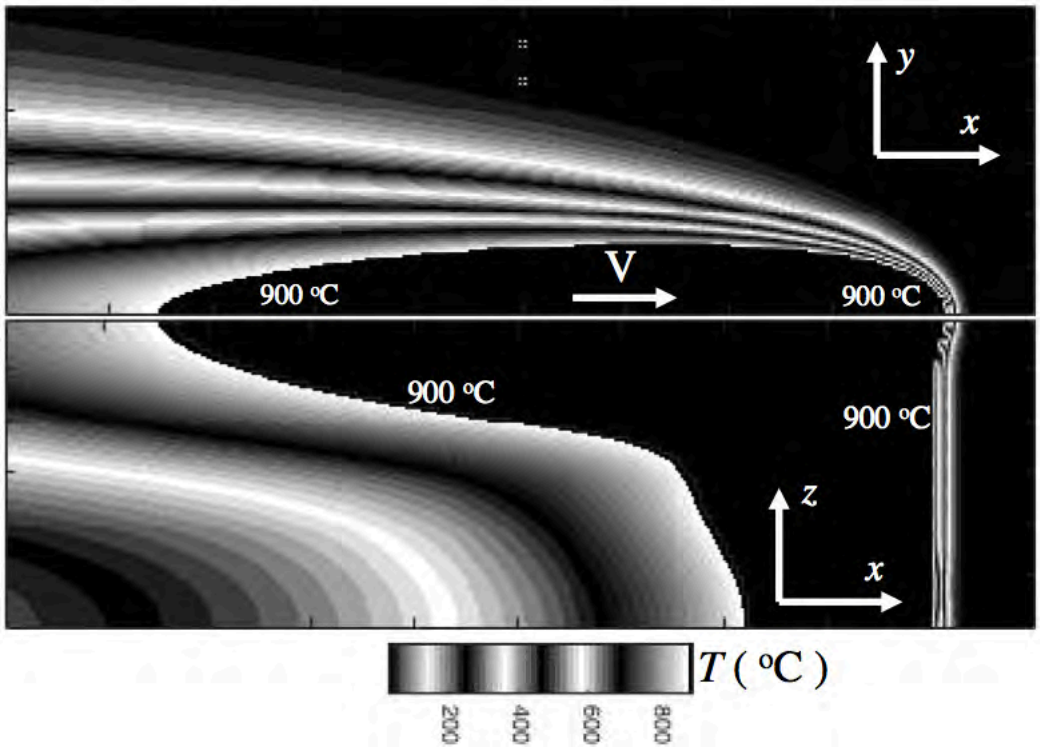

Fig. 21 Two-dimensional slices, at half workpiece top surface and longitudinal cross section at symmetry plane, of three-dimensional temperature field (^{o}C) at estimated HAZ-edge boundary calculated using constraints defined by Eq.(2), and given in Table 4 for solidification boundary (Weld 4).

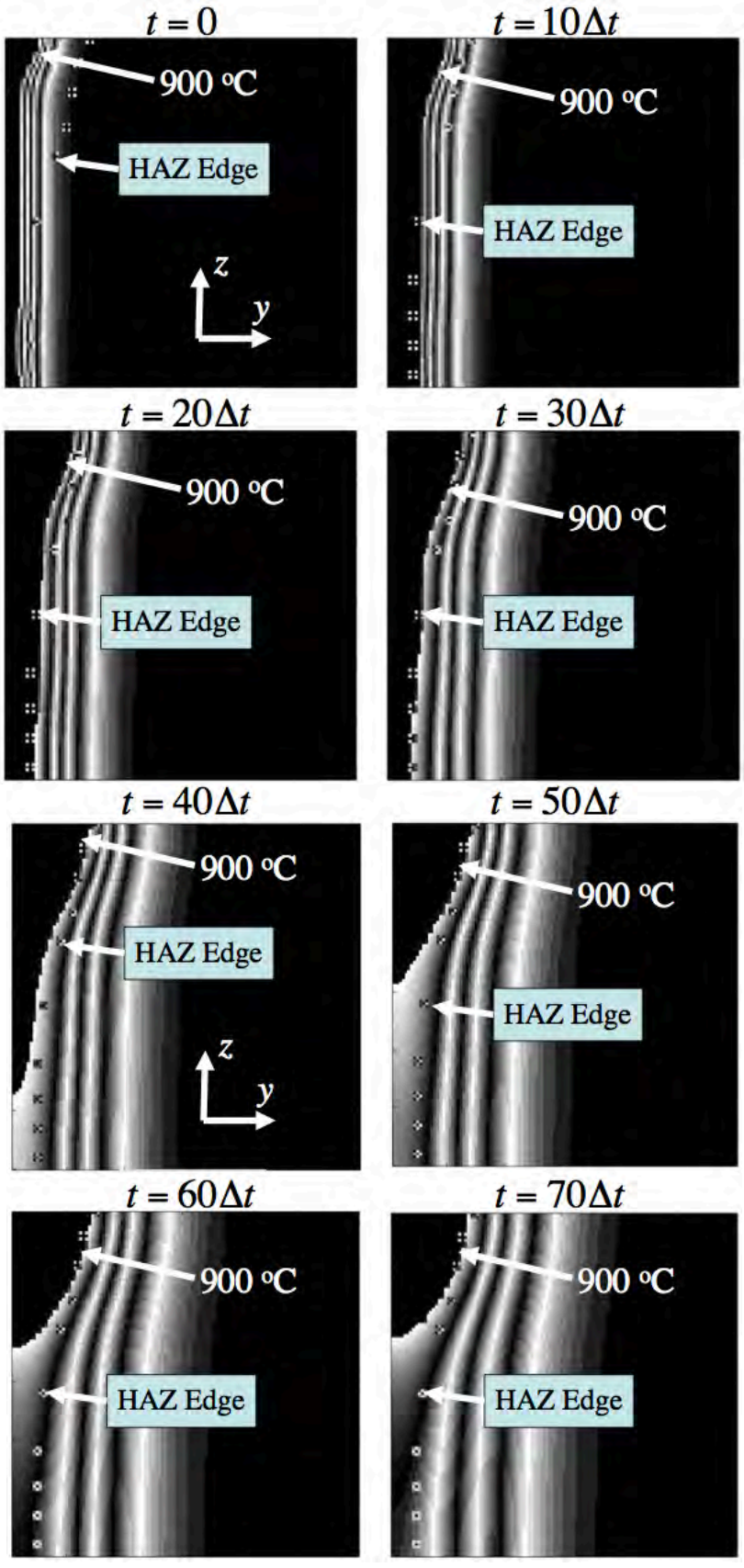
t = 0
900 °C
HAZ Edge
z
y
t = 10Δt
900 °C
HAZ Edge
t = 20Δt
900 °C
HAZ Edge
t = 30Δt
900 °C
HAZ Edge
t = 40Δt
900 °C
HAZ Edge
z
y
t = 50Δt
900 °C
HAZ Edge
t = 60Δt
900 °C
HAZ Edge
t = 70Δt
900 °C
HAZ Edge

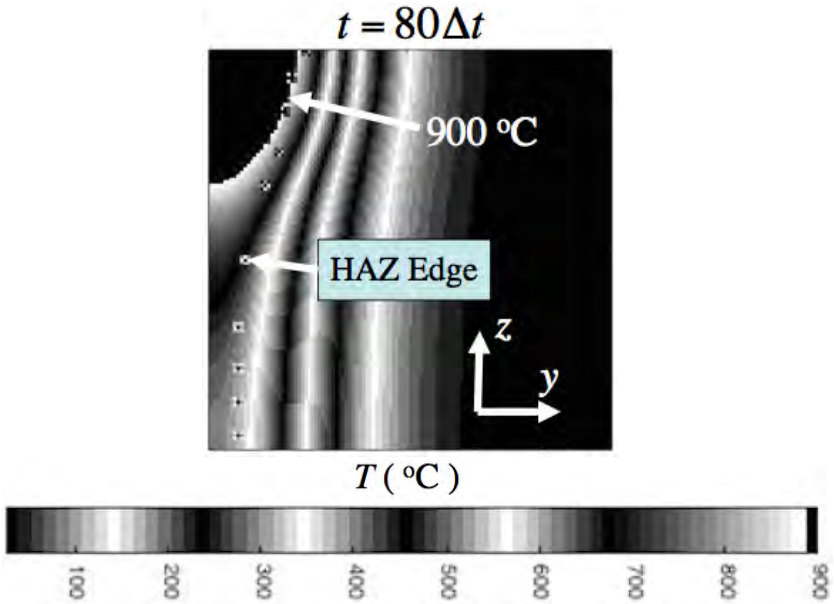

Fig. 22 Temperature history (^{o}C) at estimated HAZ-edge boundary of transverse cross section of weld calculated using constraints defined by Eq.(2) given in Table 4 for solidifcation boundary, where $\Delta t = \Delta l$ /V, Δl = (15/60) mm and V = 1.3 m/min (Weld 4).

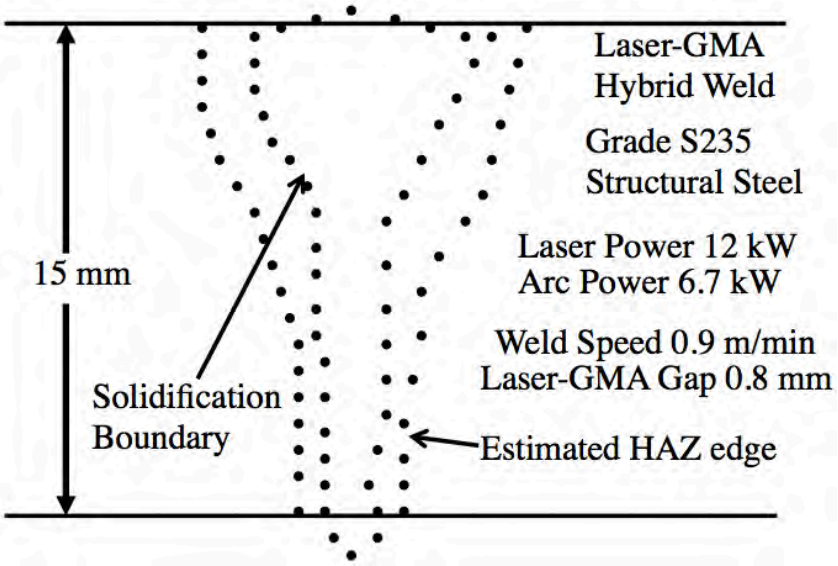

Fig. 23 Experimentally measured transverse weld cross sections of solidification and HAZ-edge boundaries for steel laser-GMA hybrid weld (Weld 5).

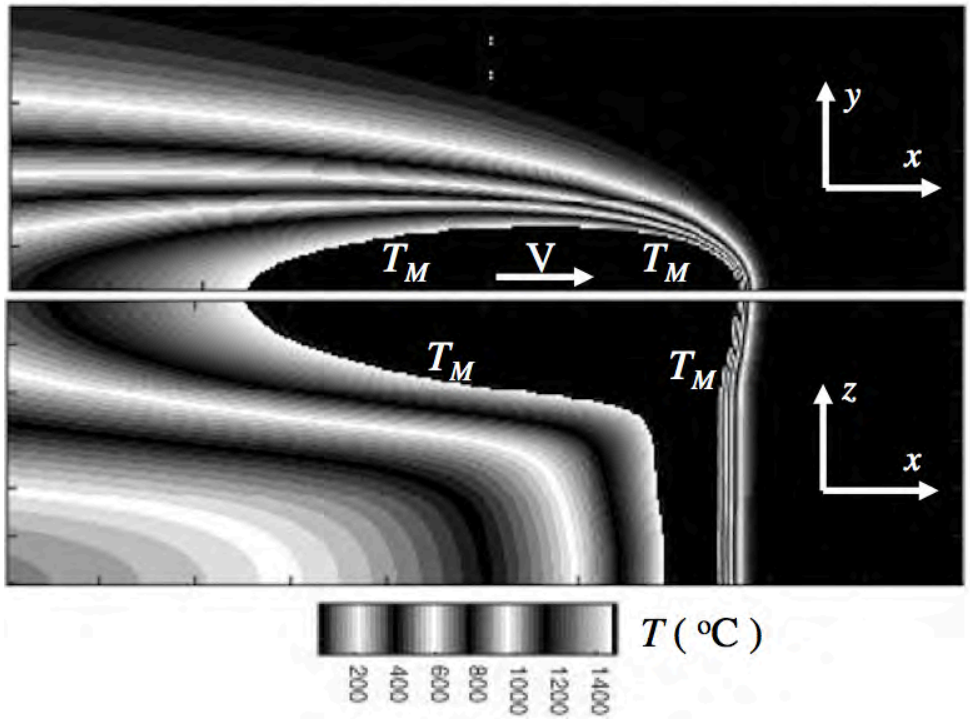

Fig. 24 Two-dimensional slices, at half workpiece top surface and longitudinal cross section at symmetry plane, of three-dimensional temperature field (^{o}C) calculated using cross section information given in Table 5 for solidification boundary (Weld 5).

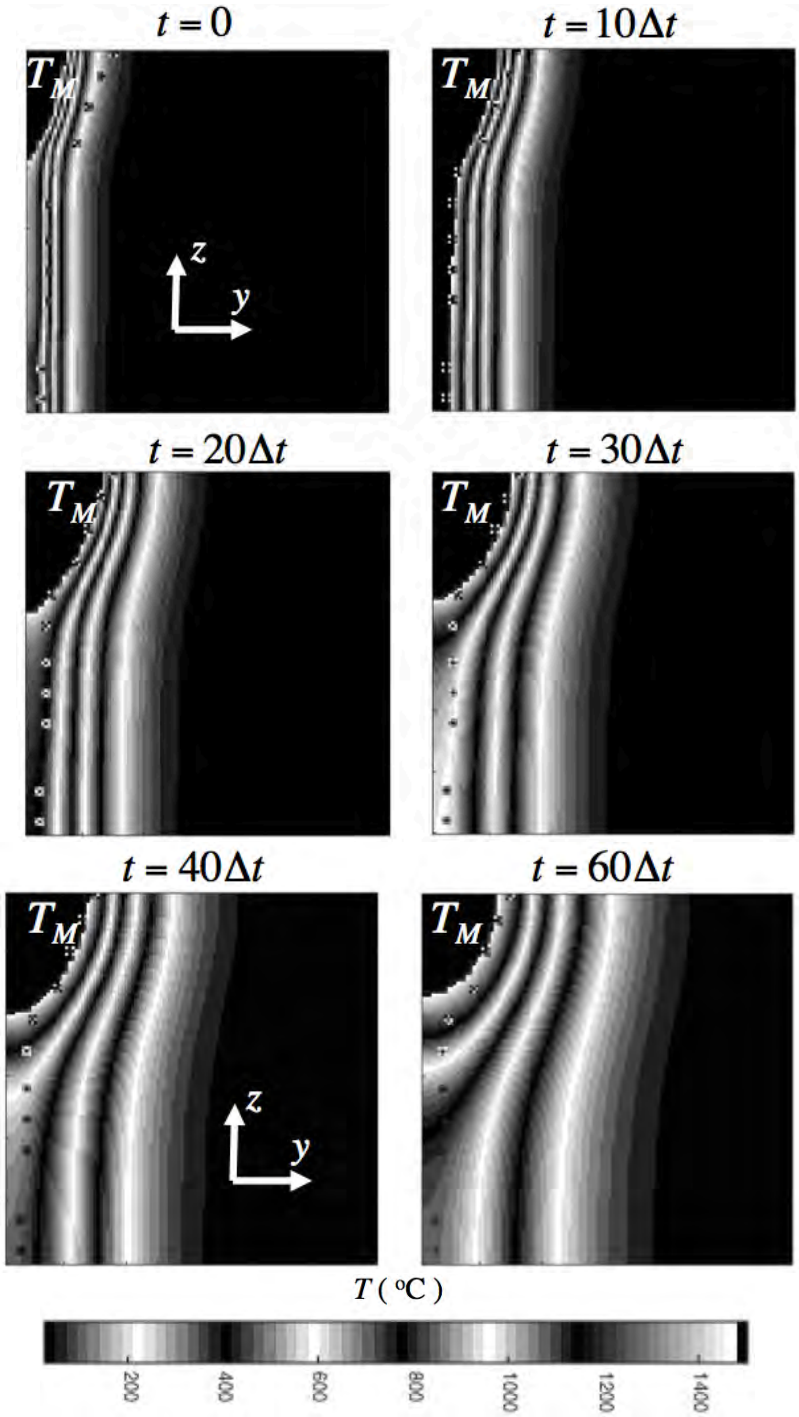

Fig. 25 Temperature history (^{o}C) of transverse cross section of weld calculated using cross section information given in Table 5 for solidification boundary, where $\Delta t = \Delta l$ /V, Δl = (15/60) mm and V = 0.9 m/min (Weld 5).

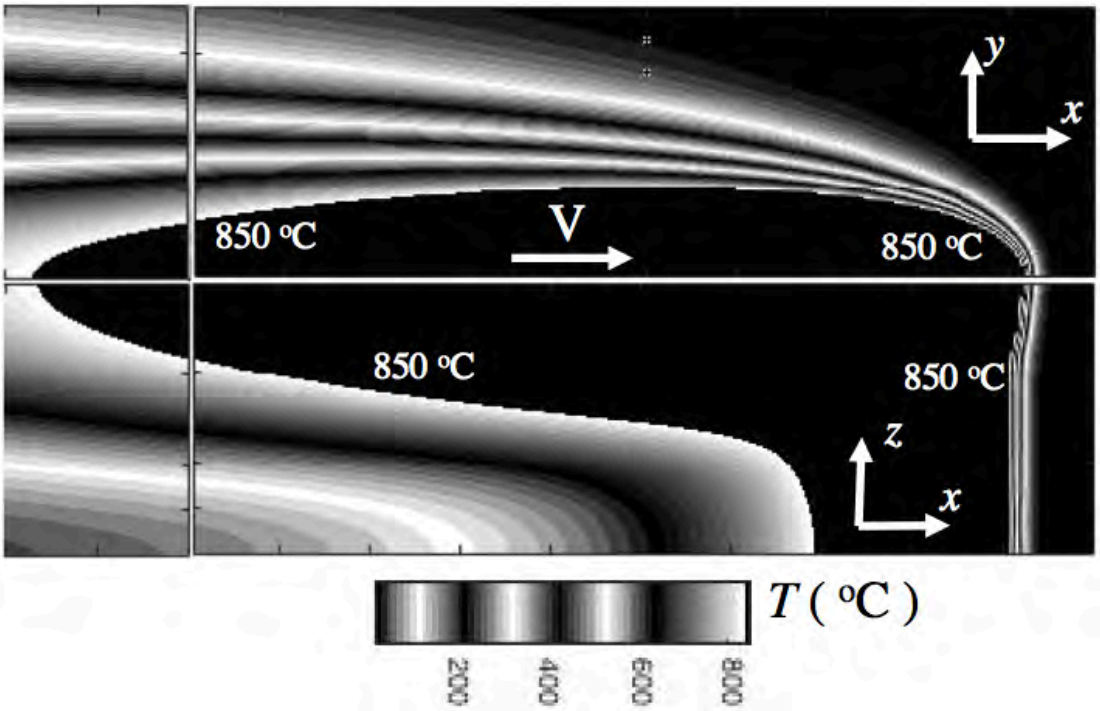

Fig. 26 Two-dimensional slices, at half workpiece top surface and longitudinal cross section at symmetry plane, of three-dimensional temperature field (^{o}C) at estimated HAZ-edge boundary calculated using constraints defined by Eq.(2), and given in Table 5 for solidification boundary (Weld 5).

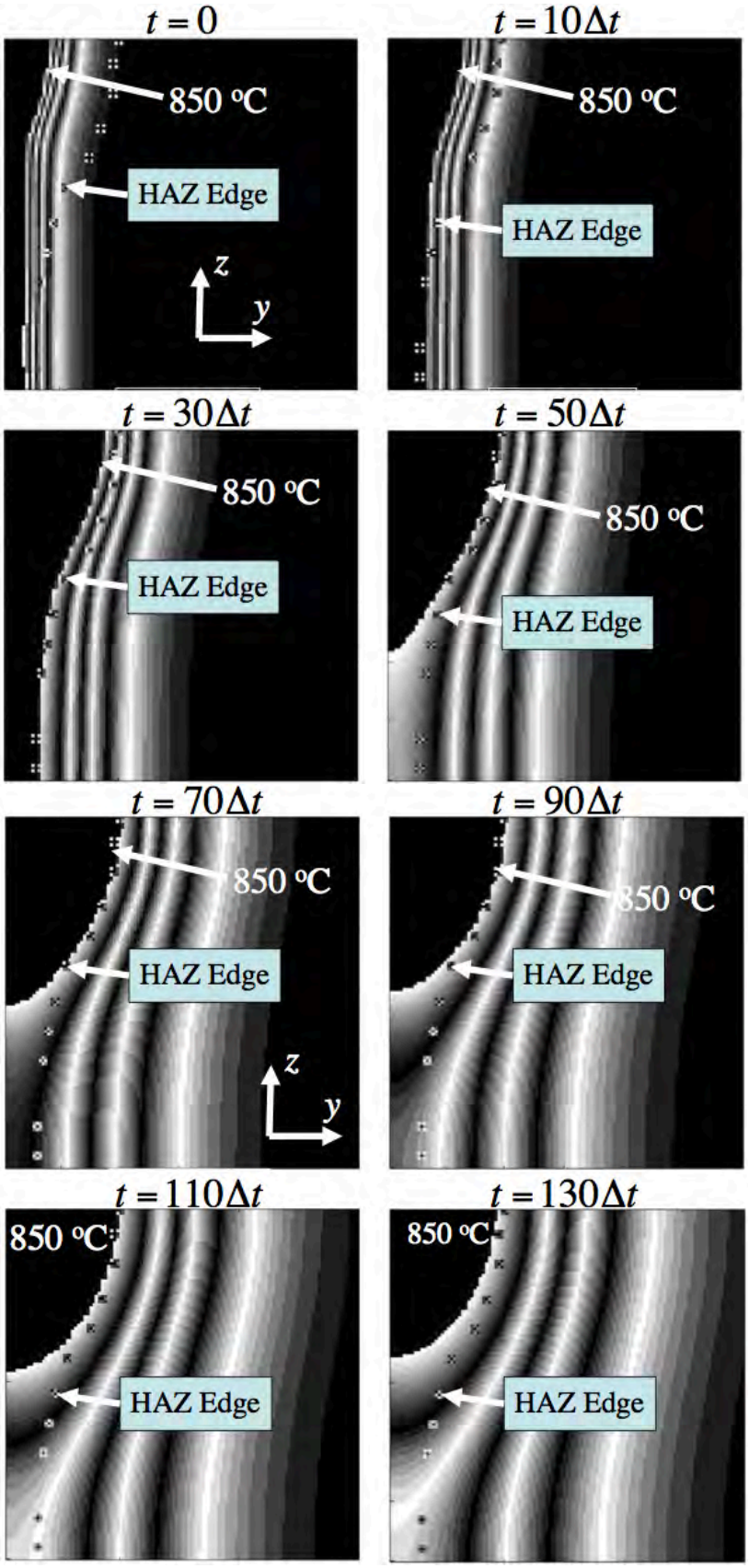
t = 0
850 °C
HAZ Edge
z
y
t = 10Δt
850 °C
HAZ Edge
t = 30Δt
850 °C
HAZ Edge
t = 50Δt
850 °C
HAZ Edge
t = 70Δt
850 °C
HAZ Edge
z
y
t = 90Δt
850 °C
HAZ Edge
t = 110Δt
850 °C
HAZ Edge
t = 130Δt
850 °C
HAZ Edge

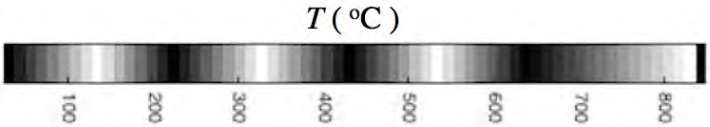

Fig. 27 Temperature history (°C) at estimated HAZ-edge boundary of transverse cross section of weld calculated using constraints defined by Eq.(2) given in Table 5 for solidifcation boundary, where $\Delta t = \Delta l$ /V, Δl = (15/60) mm and V = 0.9 m/min (Weld 5).

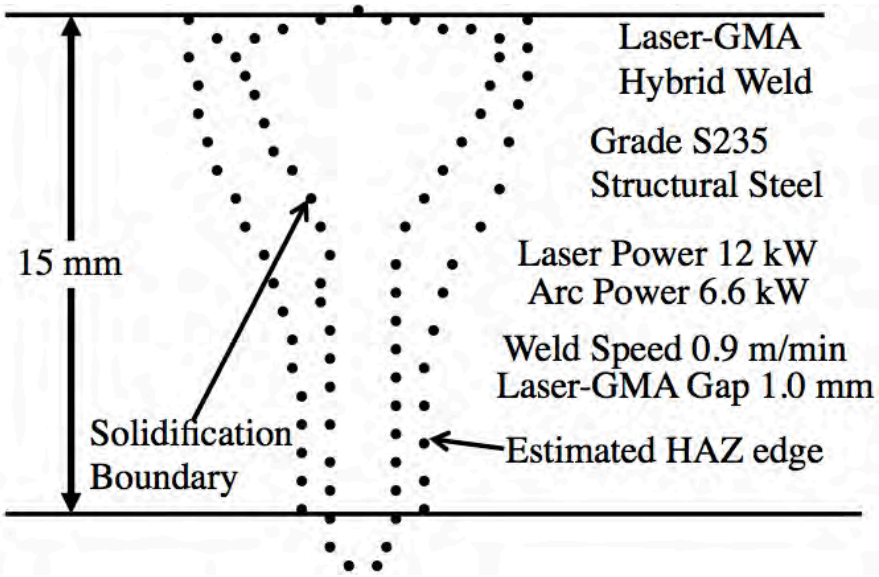

Fig. 28 Experimentally measured transverse weld cross sections of solidification and HAZ-edge boundaries for steel laser-GMA hybrid weld (Weld 6).

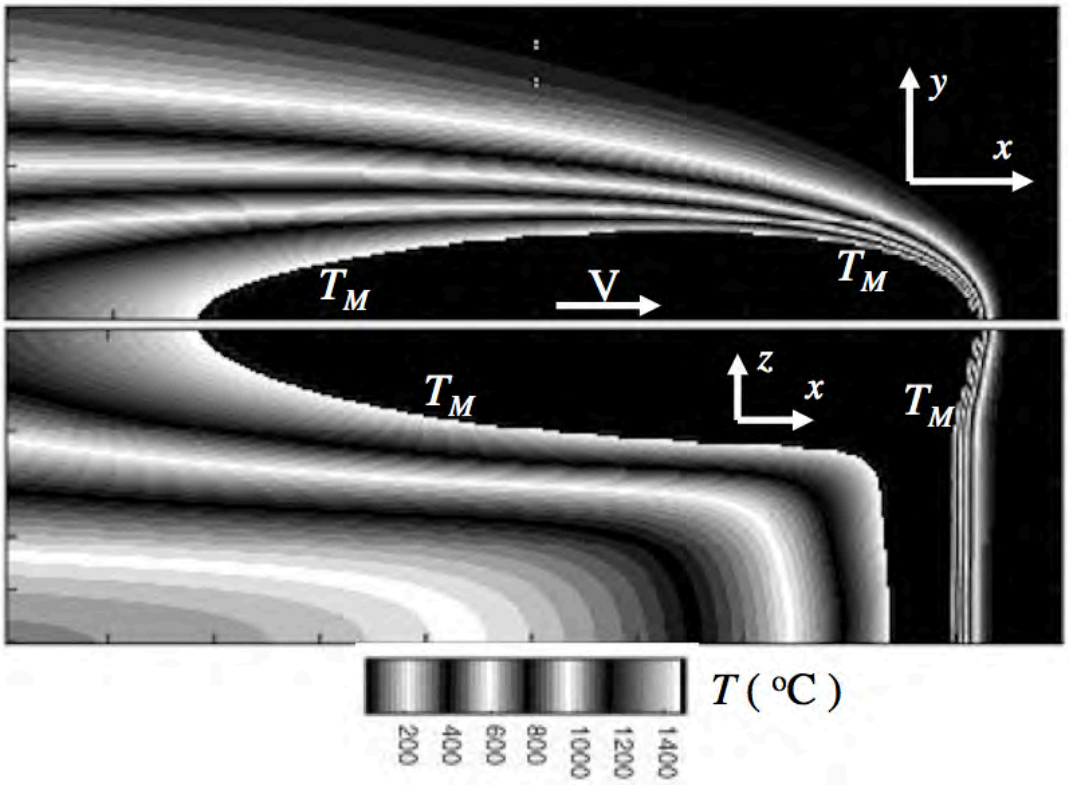

Fig. 29 Two-dimensional slices, at half workpiece top surface and longitudinal cross section at symmetry plane, of three-dimensional temperature field (^{o}C) calculated using cross section information given in Table 6 for solidification boundary (Weld 6).

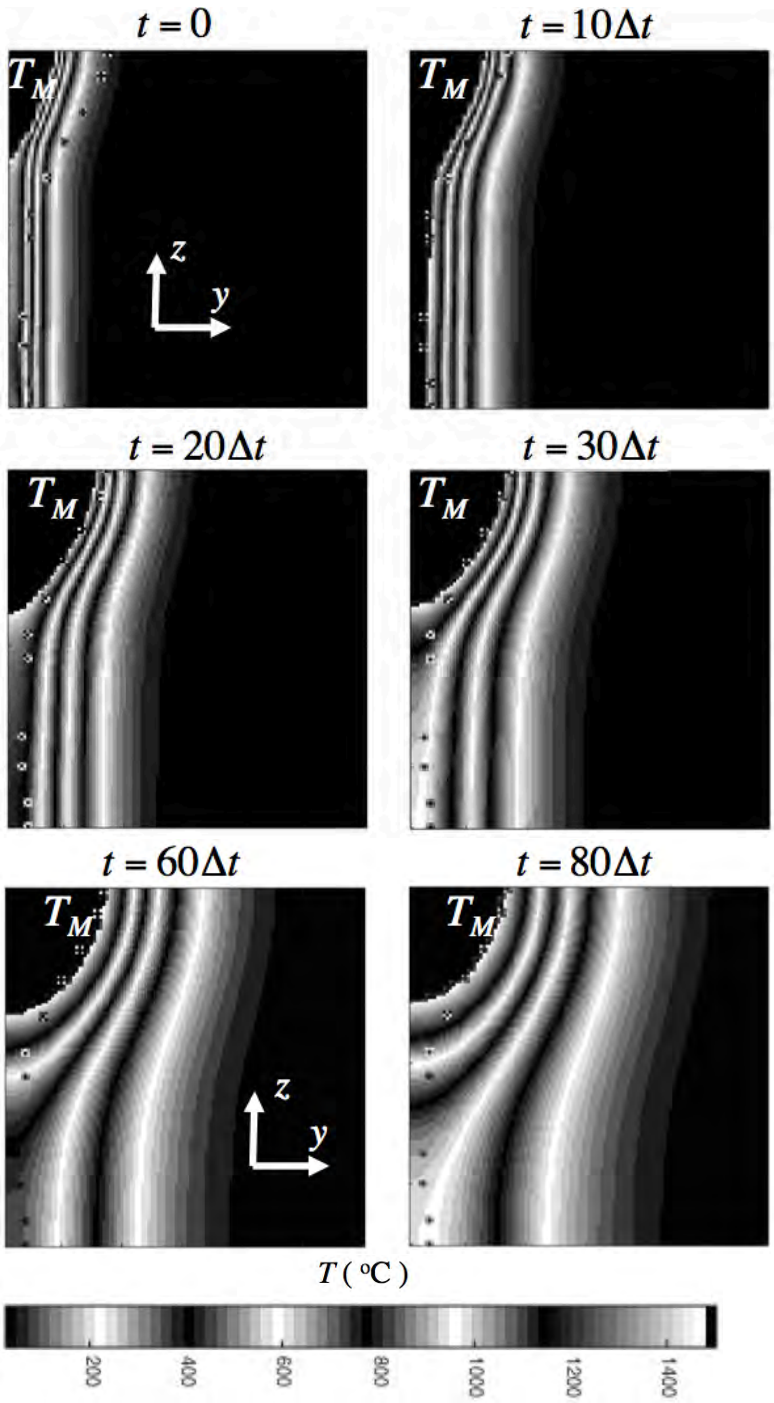

Fig. 30 Temperature history (^{o}C) of transverse cross section of weld calculated using cross section information given in Table 6 for solidification boundary, where $\Delta t = \Delta l$ /V, Δl = (15/60) mm and V = 0.9 m/min (Weld 6).

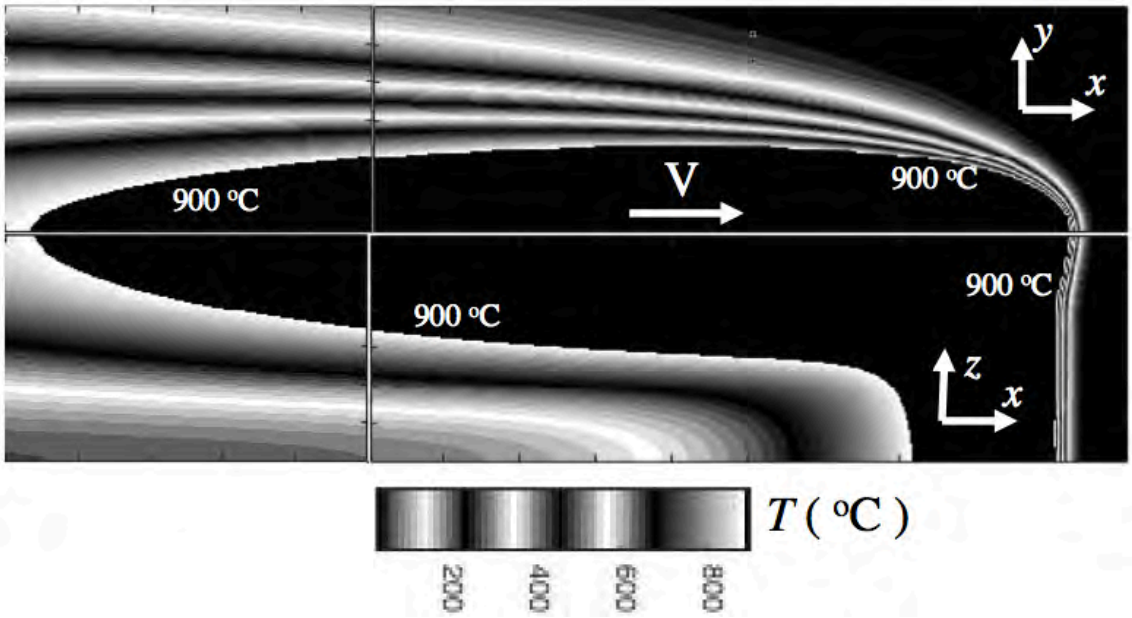

Fig. 31 Two-dimensional slices, at half workpiece top surface and longitudinal cross section at symmetry plane, of three-dimensional temperature field (^{o}C) at estimated HAZ-edge boundary calculated using constraints defined by Eq.(2), and given in Table 6 for solidification boundary (Weld 6).

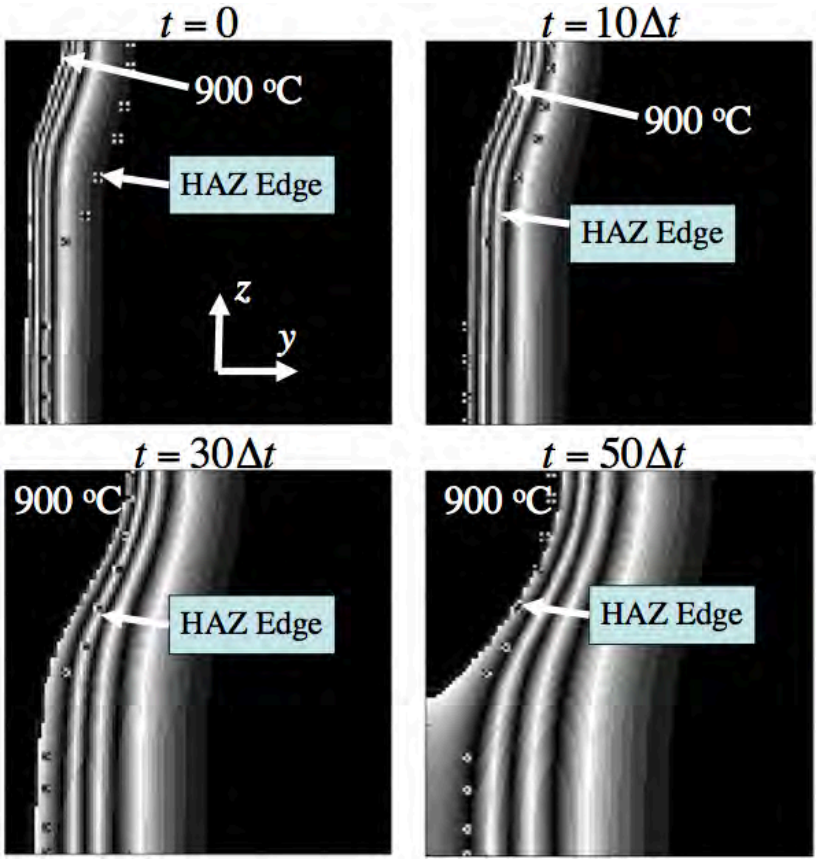

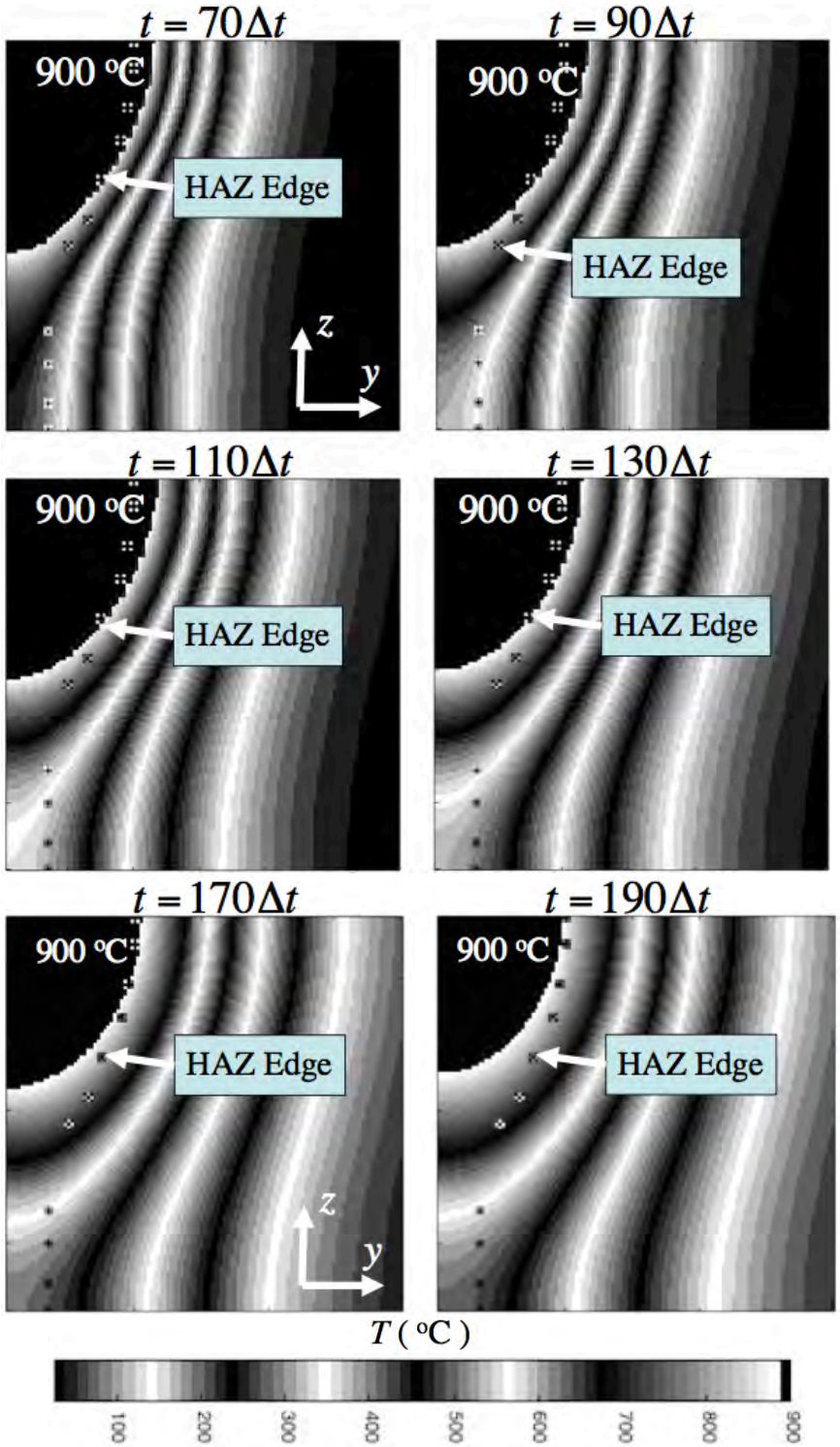

Fig. 32 Temperature history (°C) at estimated HAZ-edge boundary of transverse cross section of weld calculated using constraints defined by Eq.(2) given in Table 6 for solidifcation boundary, where $\Delta t = \Delta l$ /V, Δl = (15/60) mm and V = 0.9 m/min (Weld 6).

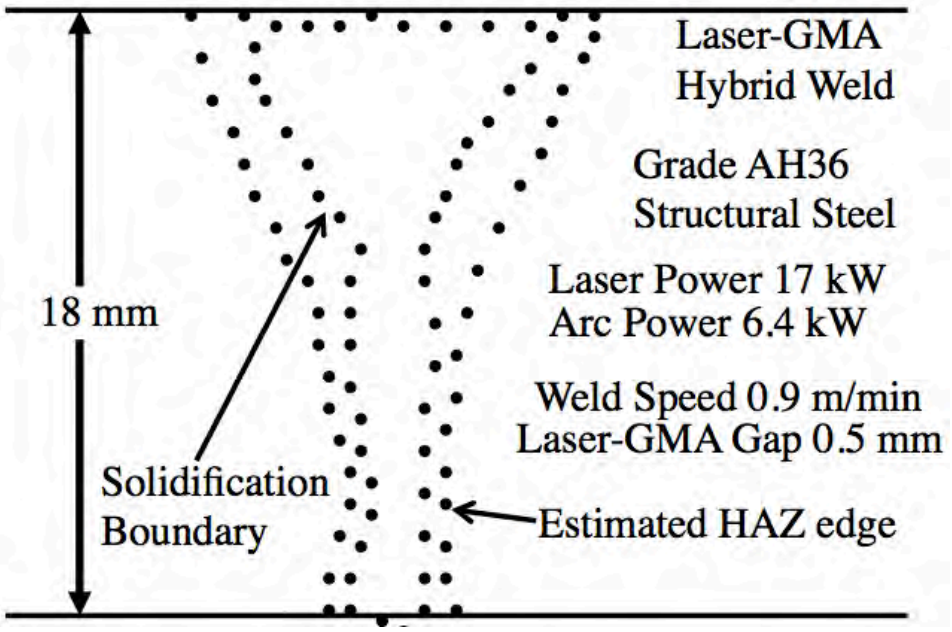

Fig. 33 Experimentally measured transverse weld cross sections of solidification and HAZ-edge boundaries for steel laser-GMA hybrid weld (Weld 7).

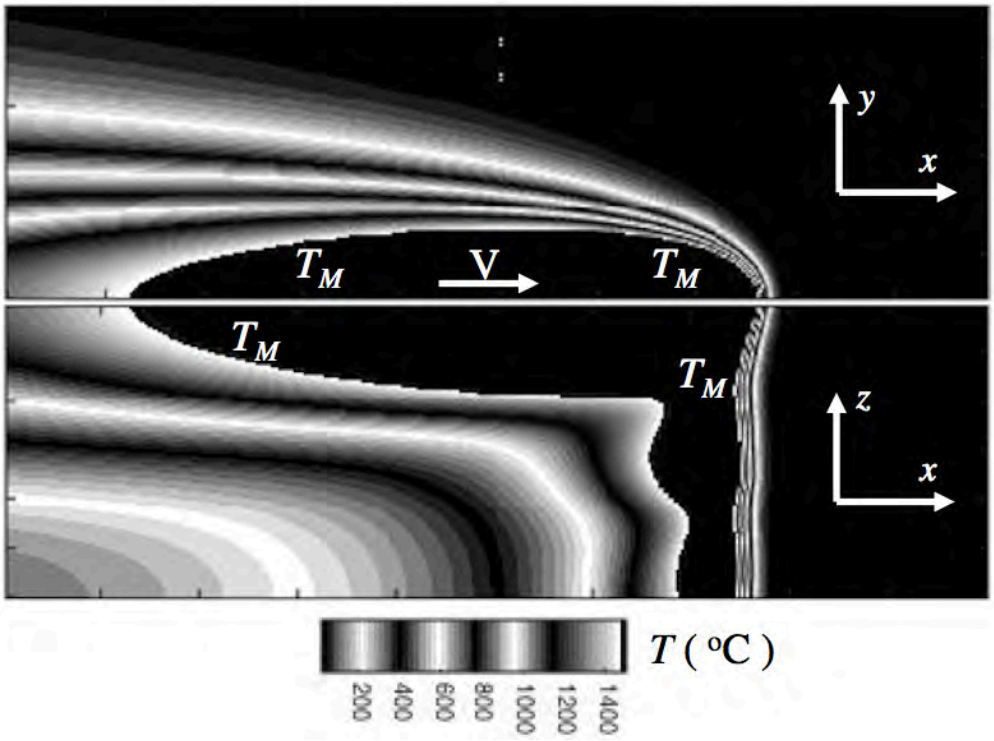

Fig. 34 Two-dimensional slices, at half workpiece top surface and longitudinal cross section at symmetry plane, of three-dimensional temperature field (^{o}C) calculated using cross section information given in Table 7 for solidification boundary (Weld 7).

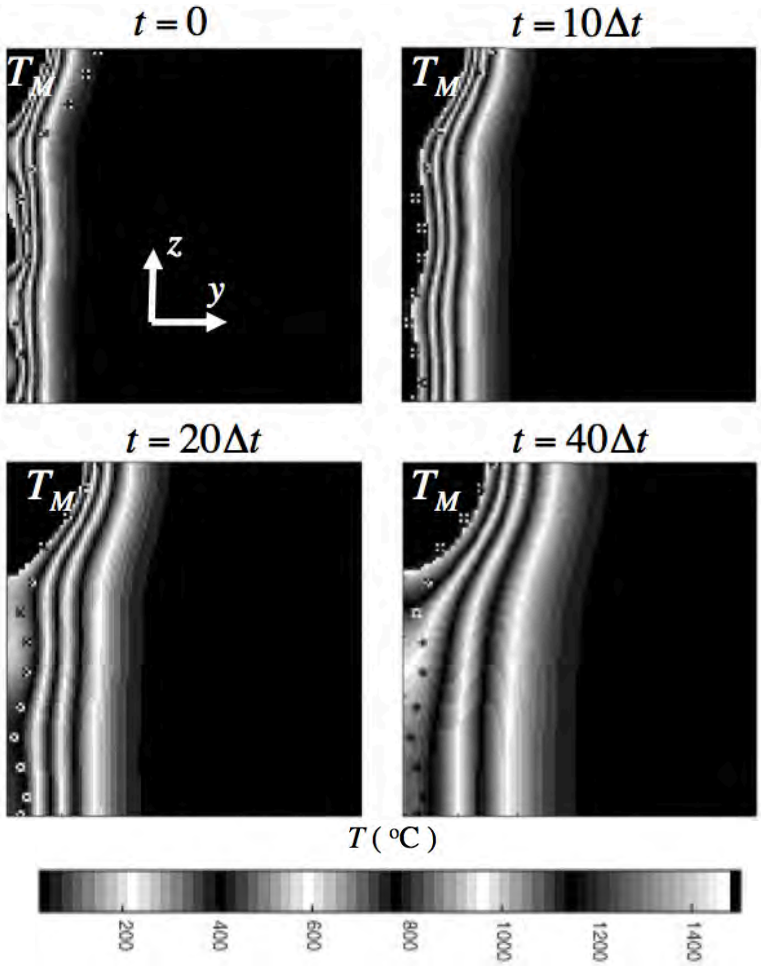

Fig. 35 Temperature history (^{o}C) of transverse cross section of weld calculated using cross section information given in Table 7 for solidification boundary, where $\Delta t = \Delta l$ /V, Δl = (18/60) mm and V = 0.9 m/min (Weld 7).

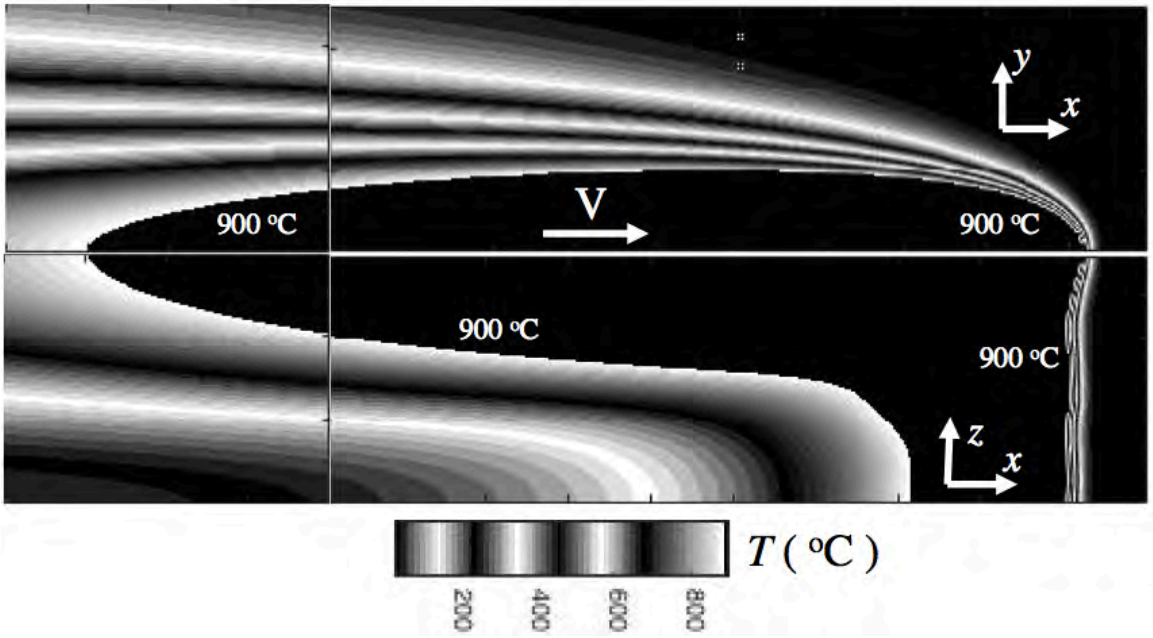

Fig. 36 Two-dimensional slices, at half workpiece top surface and longitudinal cross section at symmetry plane, of three-dimensional temperature field (^{o}C) at estimated HAZ-edge boundary calculated using constraints defined by Eq.(2), and given in Table 7 for solidification boundary (Weld 7).

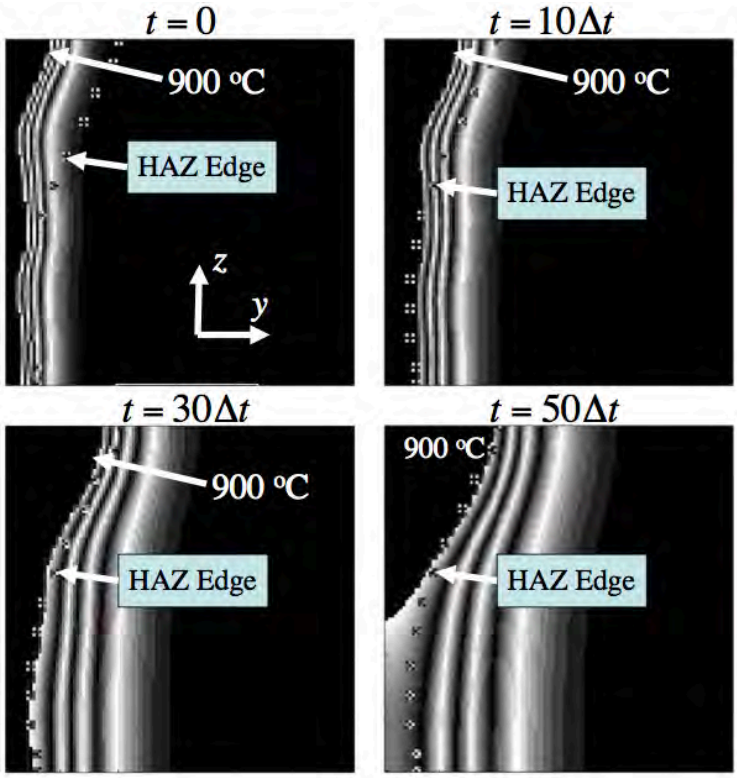

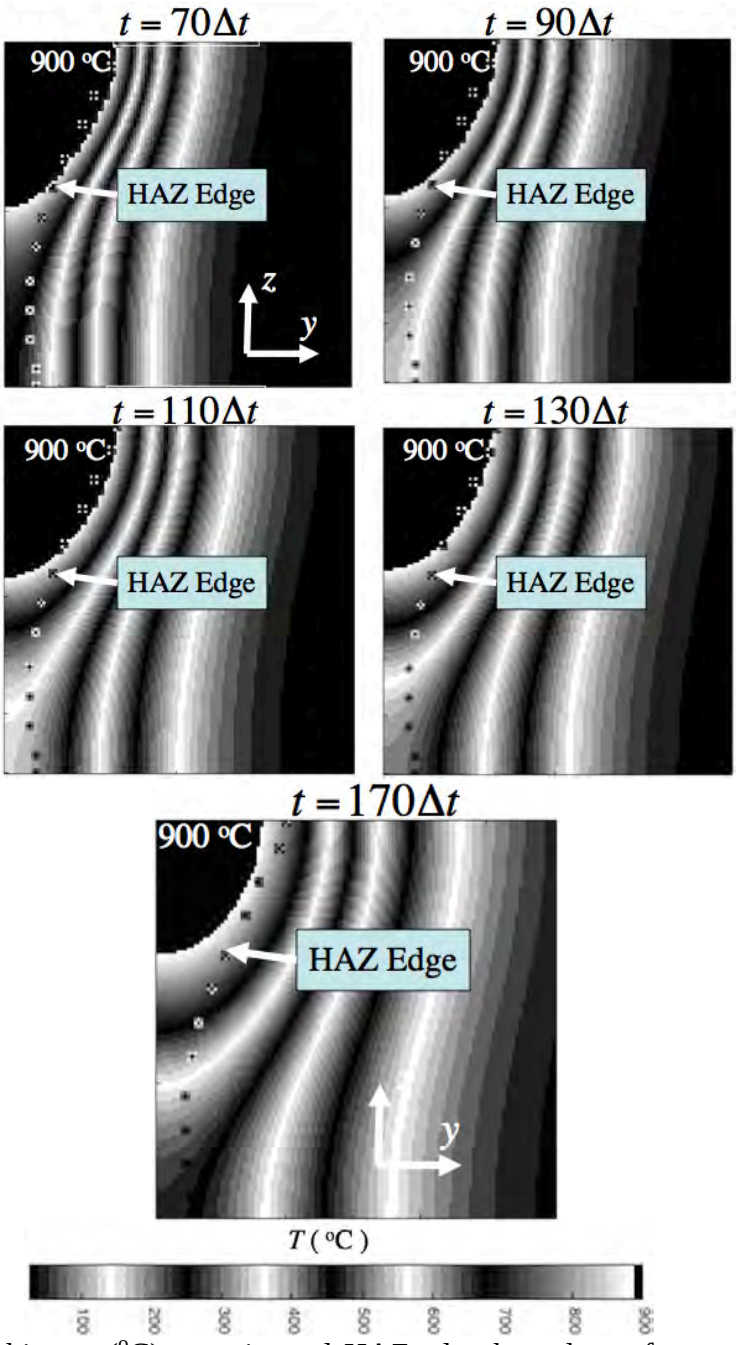

Fig. 37 Temperature history (^{o}C) at estimated HAZ-edge boundary of transverse cross section of weld calculated using constraints defined by Eq.(2) given in Table 7 for solidifcation boundary, where $\Delta t = \Delta l$ /V, Δl = (18/60) mm and V = 0.9 m/min (Weld 7).

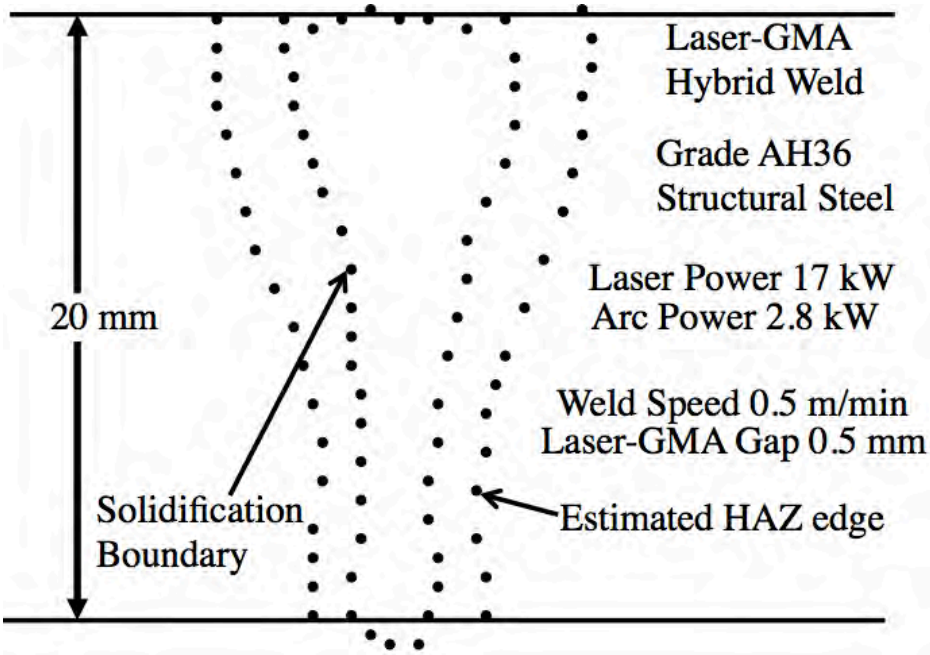

Fig. 38 Experimentally measured transverse weld cross sections of solidification and HAZ-edge boundaries for steel laser-GMA hybrid weld (Weld 8).

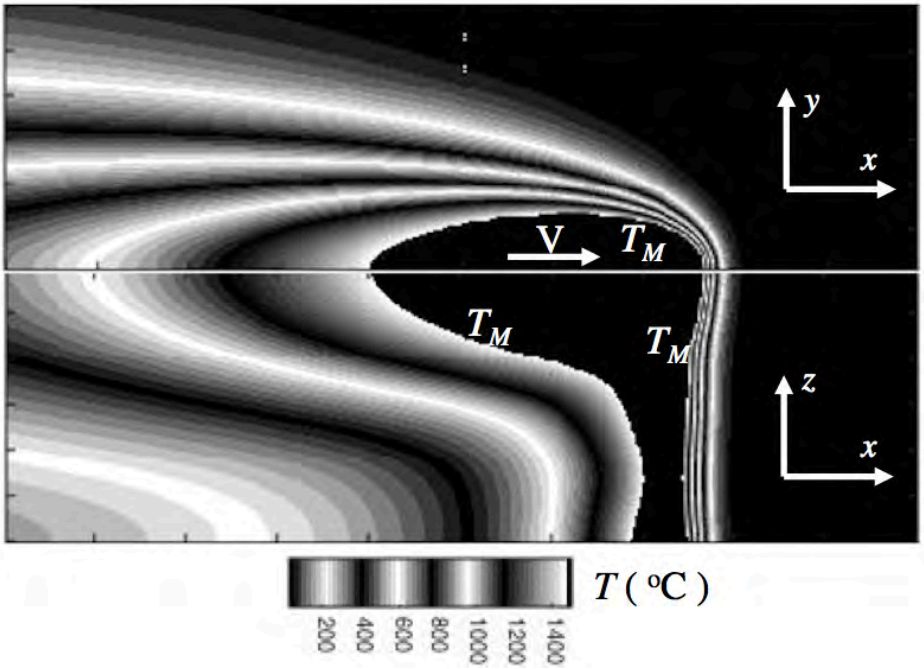

Fig. 39 Two-dimensional slices, at half workpiece top surface and longitudinal cross section at symmetry plane, of three-dimensional temperature field (^{o}C) calculated using cross section information given in Table 8 for solidification boundary (Weld 8).

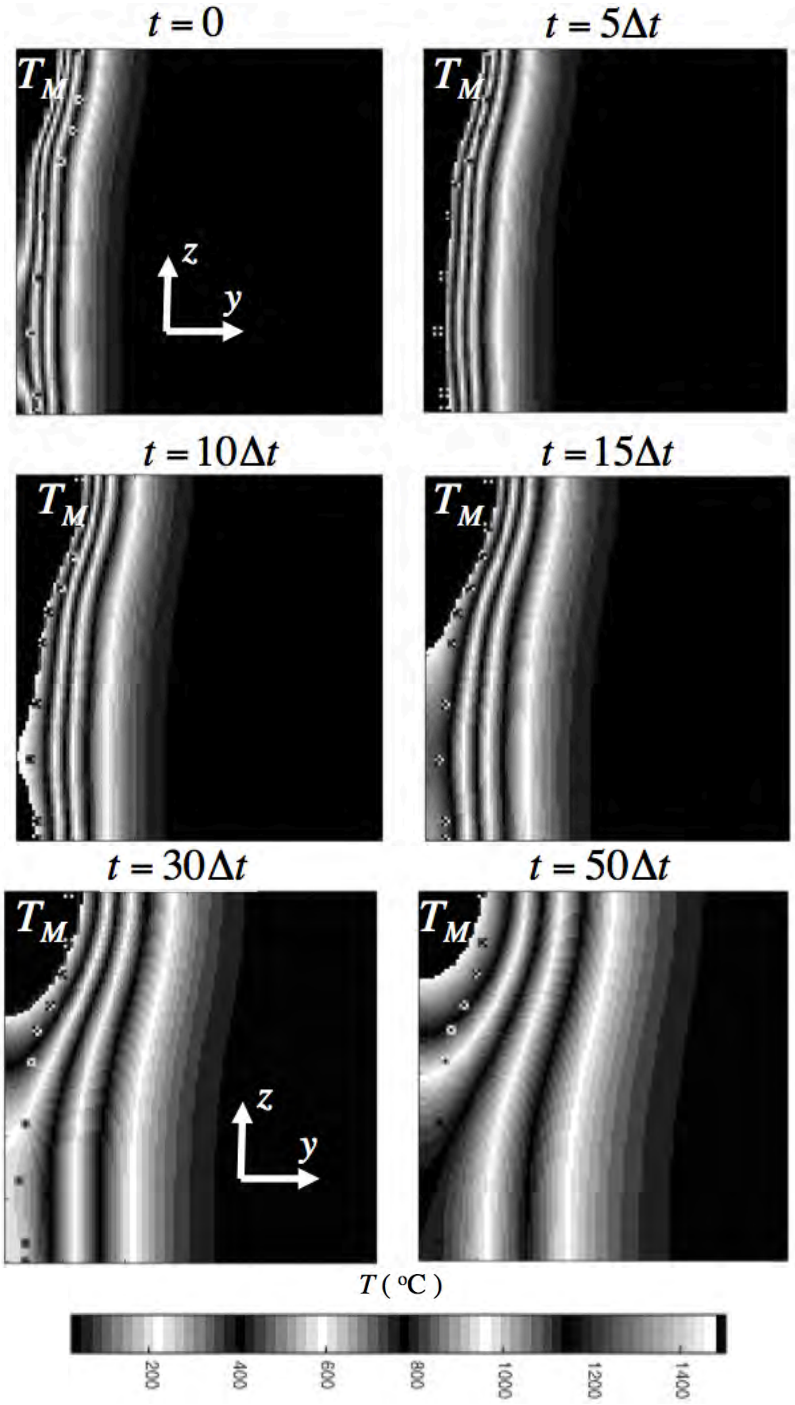

Fig. 40 Temperature history (^{o}C) of transverse cross section of weld calculated using cross section information given in Table 8 for solidification boundary, where $\Delta t = \Delta l$ /V, Δl = (20/60) mm and V = 0.5 m/min (Weld 8).

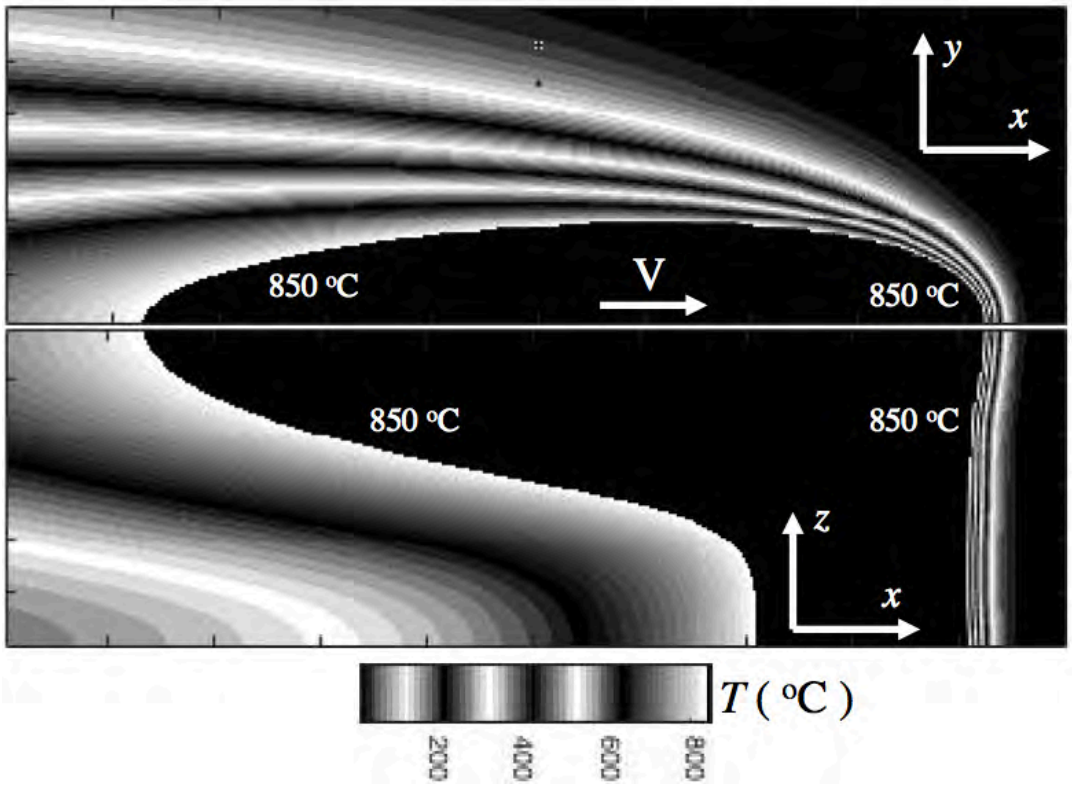

Fig. 41 Two-dimensional slices, at half workpiece top surface and longitudinal cross section at symmetry plane, of three-dimensional temperature field (^{o}C) at estimated HAZ-edge boundary calculated using constraints defined by Eq.(2), and given in Table 8 for solidification boundary (Weld 8).

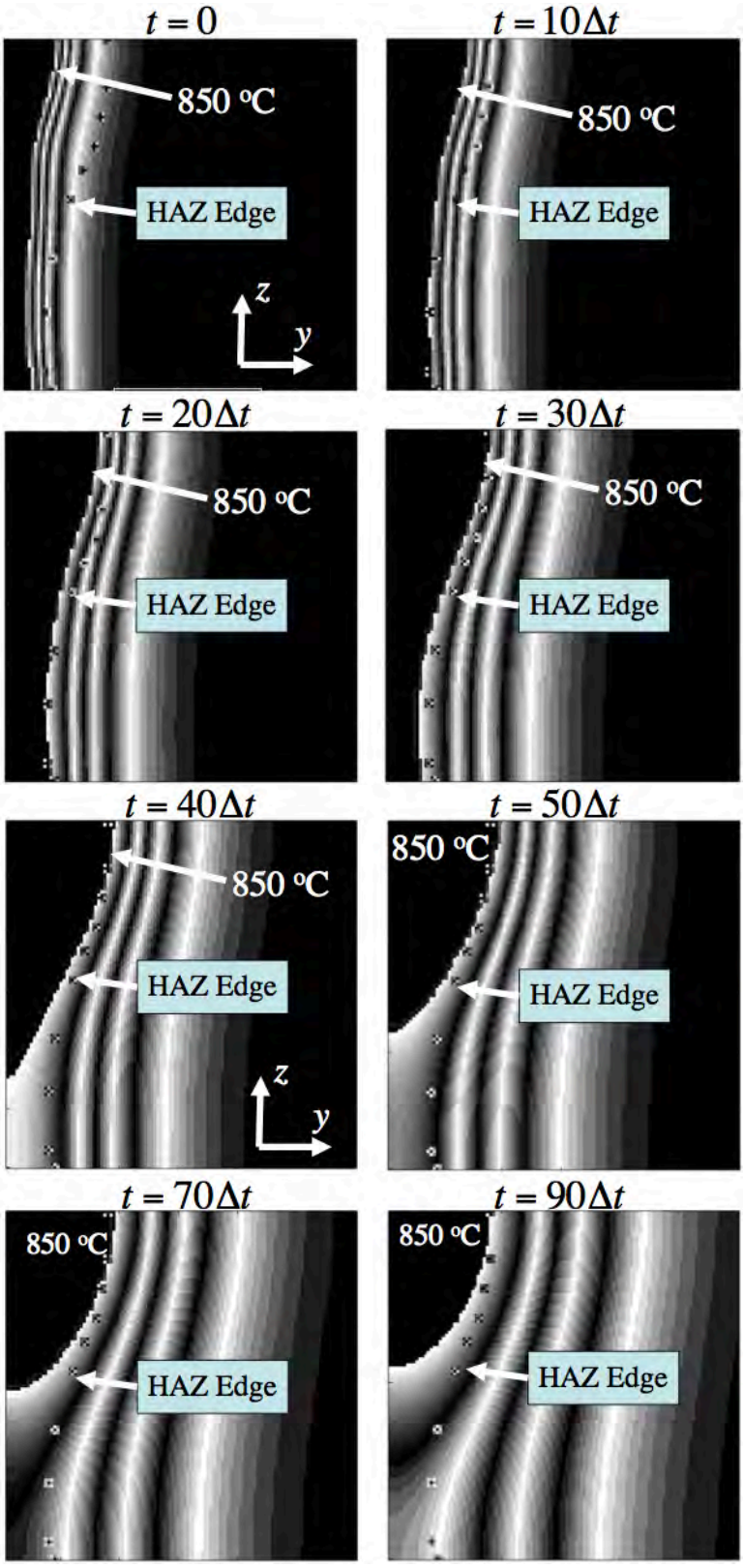
t = 0
850 °C
HAZ Edge
z
y
t = 10Δt
850 °C
HAZ Edge
t = 20Δt
850 °C
HAZ Edge
t = 30Δt
850 °C
HAZ Edge
t = 40Δt
850 °C
HAZ Edge
z
y
t = 50Δt
850 °C
HAZ Edge
t = 70Δt
850 °C
HAZ Edge
t = 90Δt
850 °C
HAZ Edge

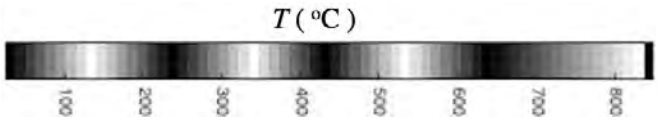

Fig. 42 Temperature history (°C) at estimated HAZ-edge boundary of transverse cross section of weld calculated using constraints defined by Eq.(2) given in Table 8 for solidifcation boundary, where $\Delta t = \Delta l$ /V, Δl = (20/60) mm and V = 0.5 m/min (Weld 8).

Discussion

The inverse analysis procedure entails calculating a three-dimensional temperature field using experimentally measured constraint conditions on the solidification boundary This temperature field permits calculation of temperature histories as a function of transverse position within the cross section of the weld. Shown in Figs. 4, 9, 14, 19, 24, 29, 34 and 39 are two-dimensional slices of the calculated three-dimensional temperature fields obtained using the constraint conditions given in Tables 1 through 8 for the measured solidification boundary, which are parallel to the relative motion of laser or laser-GMA source and workpiece. Shown in Figs. 5, 10, 15, 20, 25, 30, 35 and 40 are two-dimensional slices of this three-dimensional temperature field that are perpendicular to the relative motion of laser or laser-GMA source and workpiece. Referring to these figures, it should be noted that t = 0 has been assigned arbitrarily to a two-dimensional slice at the leading edge of the solidification boundary. Accordingly, shown in these figures is passage with time of the calculated three-dimensional solidification boundaries through experimentally measured transverse cross sections of these boundaries, which are indicated by sparse dotted contours. For the planar slices of the calculated temperature fields shown in Figs. 4, 5, 9, 10, 14, 15, 19, 20, 24, 25, 29, 30, 34, 35, 39 and 40, the weld meltpool and regions having temperatures below melting are indicated by uniform black and banded gray scale, respectively. Referring to the calculated temperature fields shown in these figures, the constraint conditions on the calculated three-dimensional solidification boundaries are such that projections of all their two-dimenional transverse slices, as a function of time, are consistent with the experimentally measured transverse cross sections of these boundaries.

Shown in Figs. 6, 11, 16, 21, 26, 31, 36 and 41 are two-dimensional slices of the calculated three-dimensional temperature field at estimated HAZ-edge boundaries obtained using the constraint conditions defined by Eq.(2), and given in Tables 1 through 8 for the solidification boundary, which are parallel to the relative motion of laser or laser-GMA source and workpiece. Shown in Figs. 7, 12, 17, 22, 27, 32, 37 and 42 are two-dimensional slices of this three-dimensional temperature field that are perpendicular to the relative motion of laser or laser-GMA source and workpiece. Again, referring to these figures, it should be noted that t = 0 has been assigned arbitrarily to a two-dimensional slice at the leading edges of the isothermal boundaries. Accordingly, shown in these figures is passage with time of the calculated three-dimensional isothermal boundaries through experimentally measured transverse cross sections of the estimated HAZ-edge boundaries, which are indicated by sparse dotted contours. For the planar slices of the calculated temperature fields shown in Figs. 6, 7, 11, 12, 16, 17, 21, 22, 26, 27, 31, 32, 36, 37, 41 and 42, regions having temperatures below and above calculated isothermal boundaries at estimated HAZ edges are indicated by uniform black and banded gray scale, respectively. Referring to the calculated temperature fields shown in these figures, it can be seen that the predicted temperature histories at cross section locations close to the experimentally estimated HAZ edge are within a range of temperatures characteristic of that for steels (see Fig. 1). That is to say, these results show reasonable consistency between model input,

solidification cross section measurements, and model output, predicted temperature histories close to the HAZ edge.

A fundamental aspect of inverse analysis methods is that errors associated with experimental measurements, which are adopted as constraints, are encoded onto the optimized values of model parameters. Accordingly, quantitative inverse analyses should consider the sensitivity of calculated field quantities with respect to measurement errors that could be associated with constraint conditions. It follows that the predicted temperature histories at the HAZ edges are expected to have errors due to the fact that, in practice, it is difficult to measure solidification and HAZ edge boundaries for steels. In particular, metallographic analysis of weld cross sections [38], using etchants, must consider the finite thickness of the mushy zone adjacent to the solidus isotherm, as well as the many different crystallographic zones in proximity of the HAZ edge (see Fig.1), which in principle may not be well defined. Thus, the inverse analysis procedure provides a consistency check with respect to experimental procedures for measurements of solidification and HAZ boundaries, for a given steel weld.

The results of this study can be adopted for more efficient inverse thermal analysis of other types of stainless steel welds. This follows in that parameter optimization can be made more efficient using initial estimates of the parameter values, which require only fine adjustment with respect to constraint conditions. Model-parameter optimization for welds, whose process parameters are within similar regimes to those for which model-parameter values have been determined previously (e.g., parameters $C(\hat{x}_k)$, $\hat{x}_k$, Δt κ and T_M for the parametric model defined by Eqs. (1)-(4)), can adopt these values as initial estimates for subsequent fine adjustment. In addition, although the thermal diffusivity κ and melt temperature T_M of steels may vary, this variation is not over a wide range of values. This is the case in general for different types metals and their alloys. It follows that parameter optimization for a specific type of steel weld, which uses initial estimates of parameter values corresponding to different types of steel welds, can adopt κ and T_M as adjustable parameters, as well as other model parameters, e.g., $C(\hat{x}_k)$, $\hat{x}_k, \Delta t$. Accordingly, the parametric temperature histories constructed according to Tables 9-16 can contribute to a parameter space containing a sufficient range of parameters corresponding to different welding processes, process conditions and different types of metals and their alloys. It follows that, given a sufficient accumulation of parameterized temperature histories, spanning a wide range of process conditions, further investigation should concern determination of an optimal structure for such a parameter space.

Finally, which should be acknowleged, there exists many different types of steels, for whose welds measurement of solidification and HAZ edge boundaries may be difficult and possibly not convenient. A classification of steels that can be characterized for quantitative estimation of solidification and HAZ edge boundaries is beyond the scope of this study. The present study indicates, however, that for steels permitting quantitative estimation of solidification and HAZ edge boundaries, temperature histories can be calculated, which are consistent with bounding temperatures of the HAZ. This consistency provides a validation of model parameter values.

Conclusion

A specific objective of this report is to further examine, for the case of structural steel welds, the concept of using experimentally measured temperature-field constraints for inverse thermal analysis. In particular, examination of a procedure for accessing the consistency of calculated temperature histories for steel welds that uses experimentally measured estimates of the HAZ edge. A general objective of this report is calculation of parametric temeprature histories by inverse thermal analysis

for structural steel deep-penetration welds corresponding to various weld process parameters. This report contributes to the continuing evolution of a parametric representation of the temperature field for inverse thermal analysis of welds associated with different types of metals, their alloys and weld process conditions

Acknowledgment

This work was supported by a Naval Research Laboratory (NRL) internal core program.

References

1. S. Kou, Welding Metallurgy, 2nd Ed., John Wiley & Sons, Inc., 2003. DOI: 10.1002/0471434027.
2. O. Grong, Metallurgical Modelling of Welding, 2ed., Materials Modelling Series, (H.K.D.H. Bhadeshia, ed.), published by The Institute of Materials, UK, (1997), chapter 2: pp. 1-115.
3. S.V. Patankar, Numerical Heat Transfer and Fluid Flow, Series in Computational Methods in Mechanics and Thermal Sciences, Hemisphere Publishing Corporation, London, 1980.
4. W.H. Press, S.A. Teukolsky, W.T. Vetterling, B. P. Flannery, Numerical Recipes in Fortran 77, The Art of Scientific Computing, 2nd Edition, Volume 1 of Fortran Numerical Recipes, Cambridge University Press, New York, 1997.
5. A. Tarantola, “Inverse Problem Theory and Methods for Model Parameter Estimation,” SIAM, Philadelphia, PA, 2005.
6. C.R. Vogel: Computational Methods for Inverse Problems, SIAM, Philadelphia, PA, 2002.
7. A. G. Ramm, Inverse Problems, Mathematical and Analytical Techniques with Applications to Engineering, Springer Science, New York, (2005).
8. J.V. Beck, B. Blackwell and C.R. St. Clair, lnverse Heat Conduction: IlI-Posed Problems, Wiley Interscience. New York, 1995.
9. O.M. Alifanov, Inverse Heat Transfer Problems, Springer,Verlag. New York, 1994.
10. M.N. Ozisik and H.R.B. Orlande, Inverse Heat Transfer, Fundamentals and Applications, Taylor and Francis, New York, 2000.
11. K. Kurpisz and A.J. Nowak, Inverse Thermal Problems, Computational Mechanics Publications, Boston, USA, 1995.
12. J.V. Beck, “Inverse Problems in Heat Transfer with Application to Solidification and Welding,” Modeling of Casting, Welding and Advanced Solidification Processes V, M. Rappaz, M.R. Ozgu and K.W. Mahin eds., The Minerals, Metals and Materials Society, 1991, pp. 427-437.
13. J.V. Beck, “Inverse Problems in Heat Transfer,” Mathematics of Heat Transfer, G.E. Tupholme and A.S. Wood eds., Clarendon Press, (1998), pp. 13-24.
14. A.N. Tikhonov, "Inverse Problems in Heat Conduction,” J. Eng. Phys., 29(1), 816-820,1975.
15. O.M. Alifanov, “Solution of an Inverse Problem of Heat-Conduction by Iterative Methods,” J. Eng. Phys., 26(4), 471-476, 1974.
16. O.M. Alifanov and V.Y. Mikhailov, "Solution of the Overdetermined Inverse Problem of Thermal Conductivity Involving Inaccurate Data,” High Temperature, 23(1), 112-117, 1985.
17. E.A. Artyukhin and A.V. Nenarokomov, “Coefficient Inverse Heat Conduction Problem,” J. Eng. Phys.. 53,1085-1090, 1988.
18. T.J. Martin and G.S. Dulikravich, “Inverse Determination of Steady Convective Local Heat Transfer Coefficients,” ASME J. Heat Transfer, 120, 328-334, 1998.

19. S.G. Lambrakos and S.G. Michopoulos, Algorithms for Inverse Analysis of Heat Deposition Processes, 'Mathematical Modelling of Weld Phenomena,' Volume 8, 847, Published by Verlag der Technischen Universite Graz, Austria (2007).
20. S.W. Smith, The Scientist and Engineer's Guide to Digital Signal Processing, California Technical Publishing, San Diego, California, 1997.
21. H. S. Carslaw and J. C. Jaegar: Conduction of Heat in Solids, Clarendon Press, Oxford, 2nd ed, 374, 1959.
22. R.W. Farebrother, Linear-Least-Square Computations, Marcel Dekker, New York, 1988.
23. Y.B. Bard, Nonlinear Parameter Estimation, Academic Press, New York. 1974.
24. S.G. Lambrakos and J.O. Milewski, Analysis of Welding and Heat Deposition Processes using an Inverse-Problem Approach, Mathematical Modelling of Weld Phenomena, **7**, 1025, Publishied by Verlag der Technischen Universite Graz, Austria 2005, pp. 1025-1055.
25. S.G. Lambrakos, "Inverse Thermal Analysis of 304L Stainless Steel Laser Welds," J. Mater. Eng. And Perform., 22(8), 2141 (2013).
26. S.G. Lambrakos, "Inverse Thermal Analysis of Stainless Steel Deep-Penetration Welds Using Volumetric Constraints," Journal of Materials Engineering and Performance, published online 2014, DOI: 10.1007/s11665-014-1023-7, Volume 23(6), June 2014, pp. 2219-2232.
27. S.G. Lambrakos, "Inverse Thermal Analysis of Welds Using Multiple Constraints and Relaxed Parameter Optimization," Journal of Materials Engineering and Performance, Volume 24(8) August 2015, pp. 2925-2936.
28. D. Rosenthal, "The theory of moving sources of heat and its application to metal treatments," Trans ASME, Vol. 68 (1946), pp. 849-866.
29. J. Goldak, A. Chakravarti and M. Bibby, "A new finite element model for welding heat source," Metall. Trans. B, Vol. 15, pp. 299-305, 1984.
30. R.O. Myhr and O. Grong,'Acta Metall. Mater., 38, 1990, pp. 449-460.
31. R.C. Reed and H.K.D.H Bhadeshia: "A Simple Model For Multipass Welds," Acta Metall. Mater. 1994, 42(11), 3663-3678.
32. V.A. Karkhin, P.N. Homich and V.G. Michailov, "Models for Volume Heat Sources and Functional-Analytic Technique for Calculating the Temperature Fields in Butt Welding, 'Mathematical Modelling of Weld Phenomena,' Volume 8, 847, Published by Verlag der Technischen Universite Graz, Austria (2007).
33. A.A. Deshpande, A. Short, W. Sun, D.G. McCartney, L. Xu and T.H. Hyde, "Finite-Element Analysis of Experimentally Identified Parametric Envelopes for Stable Keyhole Plasma Arc Welding of a Titanium Alloy," Journal of Strain Analysis for Engineering Design, 47(5), pp. 266-275, 2012.
34. I.S. Leoveanu, G. Zgura, D. Birsan, "Modeling the Heat and Fluid Flow in the Welded Pool," Bulletin of the Transsilvania University of Brasov, Vol. 3, pp. 363-368, ISSN 1223-9631, 2007.
35. I.S. Leoveanu and G. Zgura, "Modelling the Heat and Fluid Flow in the Welded Pool from High Power Arc Sources," Materials Science Forum, Editors: C. Lee, J-B. Lee, D-H. Park, S-J. Na, Vols. 580-582, pp.443-446, 2008.
36. J. K. Kristensen, "Laser and Hybrid Laser-GMA Welding of Structural Steels, A Challenge to Research and Industry for Two Decades," Trends in Welding Research, Proceedings of the 8th International Conference, Editors: S.A. David, T. DebRoy, J.N. DuPont, T. Koseki, H.B. Smartt, ASM International, 645-641, 2009.

37. S.G. Lambrakos and A. Shabaev, “Temperature Histories of Ti-6Al-4V Pulsed-Mode Laser Welds Calculated Using Multiple Constraints,” Naval Research Laboratory Memorandum Report, Naval Research Laboratory, Washington, DC, NRL/MR/6390--15-9621 (August 12, 2015).
38. E.A. Metzbower, D.W. Moon, C.R. Feng, S.G. Lambrakos and R.J. Wong: “Modelling of HSLA-65 GMAW Welds,” Mathematical Modelling of Weld Phenomena, *7*, Publishied by Verlag der Technischen Universite Graz, Austria, pp. 327-339 (2005).